Input rate encoding and gain control in dendrites of neocortical pyramidal neurons

Nikolai C. Dembrow[1,2], **William J. Spain**[1,2,3,4,*]

[1]Epilepsy Center of Excellence, Veterans Affairs Puget Sound Healthcare System, Seattle, WA 98108, USA

[2]Department of Physiology & Biophysics, University of Washington, Seattle, WA 98195, USA

[3]Department of Neurology, University of Washington, Seattle, WA 98195, USA

[4]Lead contact

SUMMARY

Elucidating how neurons encode network activity is essential to understanding how the brain processes information. Neocortical pyramidal cells receive excitatory input onto spines distributed along dendritic branches. Local dendritic branch nonlinearities can boost the response to spatially clustered and synchronous input, but how this translates into the integration of patterns of ongoing activity remains unclear. To examine dendritic integration under naturalistic stimulus regimes, we use two-photon glutamate uncaging to repeatedly activate multiple dendritic spines at random intervals. In the proximal dendrites of two populations of layer 5 pyramidal neurons in the mouse motor cortex, spatially restricted synchrony is not a prerequisite for dendritic boosting. Branches encode afferent inputs with distinct rate sensitivities depending upon cell and branch type. Thus, inputs distributed along a dendritic branch can recruit supralinear boosting and the window of this nonlinearity may provide a mechanism by which dendrites can preferentially amplify slow-frequency network oscillations.

Graphical Abstract

Measure the voltage response to random naturalistic patterns of dendritic spine stimulation:

Total input rate drives supralinear events

An input-rate based model of dendritic integration

Slow network oscillations are amplified by dendrites

In brief

Using repetitive activation of multiple spines distributed along a dendritic branch in neocortical pyramidal neurons, Dembrow and Spain demonstrate that supralinear dendritic boosting depends upon the combined activation rate of spines along a dendritic branch. A rate-based model suggests that such supralinear integration provides amplification of slow network oscillations.

INTRODUCTION

Neuronal networks exhibit a wide range of activity patterns. As our understanding improves regarding how neuronal assemblies drive behaviorally relevant network activity (Aeed et al., 2020; Li et al., 2015, 2016; Meyer et al., 2018; Takahashi et al., 2020; Taxidis et al., 2020), an equally important question remains unresolved: How is network activity coded at the level of a single neuron? Theoretical and experimental work suggest that neurons may encode information in the rate and/or the precise timing of action potentials (Brette, 2015; Dayan and Abbott, 2001; Shadlen and Newsome, 1994; Reike et al., 1999). Whether neurons utilize rate or temporal coding, spike activity must be interpreted by down-stream targets. How this functions remains elusive. For pyramidal neurons, interpreting afferent activity is particularly complex as they receive thousands of excitatory inputs throughout their extensive dendritic arbor. Individual dendritic branches can act as computational subunits, locally integrating tens to hundreds of excitatory inputs and these computations are shaped by nonlinearities from voltage-gated ion channels and synaptic voltage-sensitive NMDA receptors (Antic et al., 2010; Branco and Häusser, 2010, 2011; Harnett et al., 2012; Larkum et al., 2009; Llinás and Sugimori, 1980; Losonczy and Magee, 2006; Losonczy et

al., 2008; Major et al., 2008, 2013; Makara and Magee, 2013; Nevian et al., 2007; Papoutsi et al., 2014; Poleg-Polsky, 2015; Polsky et al., 2009; Schiller et al., 2000).

Previously, dendritic integration at the resolution of individual spines has been tested experimentally under highly constrained conditions: when clustered inputs are each activated only once. In such experiments, supralinear boosting primarily occurs if a sufficient number of clustered spines are activated near synchronously (Branco and Häusser, 2011; Harnett et al., 2012; Larkum et al., 2009; Losonczy and Magee, 2006; Losonczy et al., 2008; Makara and Magee, 2013; Schiller et al., 2000). However, neocortical networks exhibit activity regimes in which many neurons fire repeatedly for prolonged periods. Continuous network activity is exemplified in the primary motor cortex, which exhibits oscillations during the planning and execution of movement wherein neurons can fire at high rates (10–40 Hz) for several seconds (Castro-Alamancos, 2013; Cheney et al., 1991; Davis et al., 2012; Fisher et al., 2016). During these periods, multiple inputs to individual dendritic branches are repeatedly active, albeit not necessarily sharply correlated with one another in time. Predictions from both biophysical and statistical models in silica suggest that spines activated near-simultaneously are unlikely to generalize to more complex stimulation paradigms (Ujfalussy et al., 2015, 2018), but this remains untested experimentally.

Here, we tested how thin-caliber dendrites proximal to the soma (basal and proximal apical oblique dendrites) of two different classes of layer 5 (L5) pyramidal neurons in the mouse motor cortex respond to input stimuli designed to mimic continuous activity regimes. Intratelencephalic (IT) and extratelencephalic (ET) L5 neurons possess different long-range projection patterns and intrinsic electrophysiological properties resulting in distinct computations which shape their functional roles during behavioral tasks (Baker et al., 2018; Harris and Shepherd, 2015). ET and IT neurons integrate inputs along the main apical dendrite differently (Dembrow et al., 2015; Grewe, 2010; Kalmbach et al., 2013, 2015; Takahashi et al., 2020). Whether integration in the proximal dendrites of ET versus IT neurons is also distinct remains less clear. Both neuron populations receive substantial synaptic input onto proximal dendrites (Cauller et al., 1998; Oberlaender et al., 2012; Petreanu et al., 2009), which represents the majority of the L5 recurrent excitatory input (Frick et al., 2008; Markram et al., 1997) and a substantial portion of ascending thalamic input (Meyer et al., 2010; Oberlaender et al., 2011; Rah et al., 2013; Richardson et al., 2009; Shigematsu et al., 2016). Direct comparison of branch integration of ET versus IT proximal dendrites at the level of spines remains untested. To test how these proximal compartments integrate complex patterns of ongoing input, we targeted many spines on a single proximal branch repeatedly using two-photon glutamate uncaging. The timing of glutamate photolysis at each spine occurred at random intervals, making spine stimulations uncorrelated from one another. This uncorrelated spine activation reproducibly triggered supralinear boosting even at moderate rates of stimulation (mean rates of 4–15 Hz/spine). Interspine stimulus rate was the key parameter in shaping the amplitude of supralinear responses. Using simple stimulation paradigms, in which each spine was activated only once, we determined that the rate sensitivity of the supralinearity differed from branch to branch in most dendritic compartments but was exclusively step-like in ET basal dendrites. Dendritic integration during continuous input was well captured by a simple model of input rate to output voltage, which demonstrated that steep rate sensitivity in the local dendritic processing caused a

multiplicative increase in the gain of the voltage response to slow-frequency oscillations from upstream excitatory input.

RESULTS

Branch integration in the proximal dendrites of L5 pyramidal neurons during continuous multi-spine activation

We examined dendritic integration in L5 pyramidal neurons in the motor cortex from two different mouse lines, each genetically modified to express fluorescent protein in a distinct L5 pyramidal neuron subpopulation. The Thy1-h-GFP BAC-cre line labels ET L5 pyramidal neurons and the Etv1-YFP line labels IT L5 pyramidal neurons (Groh et al., 2010; Hattox and Nelson, 2007). Fluorescently labeled neurons in the motor cortex from each line exhibited the expected somatic electrophysiological properties consistent with retrograde labeled ET and IT neurons (Figure S1).

To mimic synaptic input we utilized brief, focused pulses of light (720 nm, 0.2 ms in all experiments) to photolyze caged glutamate (2P-glu) adjacent to individual dendritic spines over a planar region of a proximal dendritic branch (representative experiment shown in Figure 1; regions with targeted spines spanned on average 62.4 ± 17.4 μm, SD, of the dendritic branch, n = 112 dendrites, see STAR Methods for details). The intensity and duration of photolyzing light was set to best match the amplitude and rise times of endogenous synaptic responses triggered by focally puffing hypertonic solution (Figure S2; Table S1; Video S1). Measured at the soma, individual EPSPs evoked from uncaging glutamate (gluEPSPs) were small in amplitude (0.27 ± 0.20 mV, mean and SD, n = 2,561, from 112 dendrites; Table S1). The response amplitude was consistent for each spine with repeated stimulation trials but varied from spine to spine (Figures 1C and S2B).

In mouse motor cortex, local pyramidal neurons providing input to the proximal dendrites exhibit elevated activity for several seconds associated with movement (3–100 Hz) (Li et al., 2015; Omlor et al., 2019; Sauerbrei et al., 2020; Sreenivasan et al., 2016). Thalamic neurons providing ascending input are also active (4–15 Hz) during these periods (Catanese and Jaeger, 2021; Poulet et al., 2012; Takahashi et al., 2021). We thus tested whether stimulus regimes designed to mimic natural patterns of synaptic input were capable of driving supralinear events. The timing of each individual spine stimulation was picked from random intervals drawn from a Poisson distribution centered around a mean rate (Figures 1D–1F). Each 2P-glu activation at every spine was uncorrelated from one another (within experimental constraints described in STAR Methods). At lower mean rates per spine (Figures 1D and 1E), voltage responses were equivalent to or less than the expected linear sum (calculated from summing the individual isolated gluEPSP of each spine in time). Higher mean stimulus rates per spine triggered supralinear responses at particular moments during the continuous spine stimulation trials (Figure 1F).

To facilitate comparisons across dendrites in which different numbers of spines could be targeted, we calculated the mean total input rate for the entire branch (e.g., 14 Hz/spine 3 29 spines = 406 Hz). Continuous stimulation regimes evoked supralinear events in both ET and IT dendrites (11/13 ET basal dendrites, 5/5 IT basal dendrites). Across all basal dendrites

tested (range of 15–43 spines, 18 basal dendrites in 14 cells), the minimum mean input rate per spine necessary to trigger supralinear responses was 6.01 ± 2.77 Hz/spine, or a mean total input rate of 191 ± 117 Hz ($\pm$ SD, n = 16 dendrites in 13 cells). This minimum rate was not different between ET or IT basal or apical oblique dendrites (23 dendrites, two-way ANOVA; $F_{(1,17)} < 1.119$; $p > 0.305$). Trials with higher stimulation rates did not exhibit significantly higher peak voltage deflections (Figure S3A; $F_{(3,51)} = 1.837$, $p = 0.1522$), but did show higher voltage areas (Figure S3B; $F_{(3,51)} = 5.048$, $p < 0.01$), consistent with more events being triggered. For similar mean total input rates, a lower percentage of ET dendrites exhibited supralinear events than IT dendrites (Figure S3C). In the dendrites that evoked supralinear events, the number of supralinear events per second saturated at lower input rates in ET compared with IT neurons (Figure S3D; Kolmogorov-Smirnov test, $p < 0.01$).

Reproducible (albeit not identical) responses to frozen inputs but not randomized ones suggested that the timing of supralinear events was the result of specific combinations of spine stimulations in time and space (Figures 1F and S4). To quantify reproducibility, we cross-correlated the voltages at each moment for trials with identical input patterns (frozen trials) to those with different input patterns (nonfrozen trials; Figure S4G). The average correlation for pairwise frozen trials was greater than for nonfrozen trials in all dendrites tested (frozen trials, $r^2 = 0.842 \pm 0.068$; nonfrozen trials, $r^2 = 0.343 \pm 0.068$, n = 7 dendrites, 5 ET basal, 2 IT basal, paired t test $p < 0.001$; Figure S4H). The average deviation in the onset times (see STAR Methods for details) of subthreshold supralinear events across frozen trials was 12.18 ± 4.66 ms (5 ET basal dendrites; Figure S4I).

The dynamics and shape of the voltage response to continuous stimulation trials depended on neuron type (Figures 2 and S3–S5). In some trials, naturalistic stimulus regimes evoked action potentials (Figure S5), but these were excluded from further analysis to focus specifically upon dendritic integration. For ET basal dendrites, supralinear events depolarized rapidly and were followed by a sharp return (Figure 2A). In contrast, most IT basal dendrites exhibited a range of amplitudes during supralinear voltage excursions (Figure 2B). While supralinear voltage responses were observed in both ET and IT neurons (Figures 2C and 2D), the phase plot trajectories (Figure 2E) indicated that ET basal dendrites integrated inputs produced an all-or-none supralinear output. In contrast, IT basal dendrites produced slow rising and graded responses that were distributed across a range of voltage amplitudes. Voltage responses in ET basal dendrites (n = 11) across all trials had higher maximal rates of rise (*dV/dt*; Figure 2F) but not peak amplitudes (Figure 2G) compared with IT basal dendrites (n = 5). Next, we compared the distribution of voltage responses in ET versus IT basal dendrites. During linear trials the distribution of voltages centered around a single peak (Figure 2H; 43 trials from 9 ET basal dendrites and 14 trials from 4 IT basal dendrites). In contrast, during trials with supralinear events, ET basal dendrites exhibited two peaks in the distribution of voltages while IT basal dendrites exhibited a broader distribution around a central peak (Figure 2I; 47 trials from 11 ET basal dendrites and 27 trials from 5 IT basal dendrites). Combined, these data suggested that ET and IT basal dendrites encoded the random, uncorrelated input during continuous spine stimulation differently.

Branch integration in the proximal dendrites of L5 pyramidal neurons with near-simultaneous activation

Differences in the voltage response during continuous spine stimulation between ET versus IT basal dendrites (Figure 2) prompted us to examine how they integrated input when each spine was activated only once. First, we tested how each neuron type responded to spines activated near-simultaneously (0.5 ms apart; Figure 3). For these experiments we expanded our investigation to include proximal apical obliques (that branched off the apical trunk <50 μm away from the soma). Supralinear responses were observed in all branch compartments (representative ex amples shown in Figure 3A). Consistent with reports where L5 cell type was not defined (reviewed in Antic et al., 2010; Major et al., 2013), the NMDA receptor was the dominant contributor to the supralinear response while Na^+ channels also partially contributed (Figures S6A–S6D).

To further characterize integration when spines were stimulated near-simultaneously, we systematically varied the number of spines activated. With a certain number of spines, evoked amplitudes became greater than the expected linear sum (IT basal dendrites, n = 21, Figures 3B and 3C; IT apical obliques, n = 11, Figure 3D; ET basal dendrites, n = 19, Figure 3E; ET apical obliques, n = 14, Figure 3F). The minimum number of spines required to elicit a supralinear voltage response (amplitude > 0.5 mV above the expected linear sum) ranged widely from dendrite to dendrite (21 ± 6 spines, n = 64 dendrites), but did not depend upon dendrite or cell type (Figure 3G; range = 7–34 spines). The variability in the number of spines necessary to evoke a supralinear response was not the result of how distributed the spines were along the dendritic branch (Figure S6G).

At the minimal number of stimulated spines necessary to evoke a supralinear response, the amplitude of the supralinearity was significantly greater in ET basal dendrites (Figures 3H and S6E). This difference was eliminated at higher spine counts as the response in IT basal and apical oblique dendrites continued to increase in amplitude (Figures 3I, S6E, and S6F). Supralinearity in ET apical oblique dendrites was weaker than in ET basal dendrites even with greater spine counts, suggesting that supralinear integration varied within ET neurons depending upon the type of proximal branch. Apical oblique dendrites examined in this study were connected to the apical trunk at distances (<50 μm) where filtering along the trunk is subtle (Dembrow et al., 2015; Gulledge and Stuart, 2003; Kalmbach et al., 2013). The total distance from the soma to the centroid of the stimulated dendritic region was not significantly different between the compartment types (ET basal, 90.7 ± 32.7 μm, n = 41; ET a.o., 112.6 ± 33.4 μm, n = 25, Kolmogorov-Smirnov test, p = 0.1098) and, as has been observed in other neuron types (Makara and Magee, 2013), the amplitude of the supralinear responses did not depend on how distributed the spines were along the dendritic branch (Figure S6H). Furthermore, cell- and branch-type differences were unlikely to be due to the density of dendritic spines for each of these compartments (see STAR Methods for quantification). It is possible that the impedance mismatch from entering the apical trunk may filter events in the apical obliques of ET neurons differently than the basal dendrites. Consistent with this, the sucrose-evoked EPSPs from the ET apical obliques were slightly smaller, but this was statistically significant (~0.05 mV difference; Wilcoxon ranked tests, p < 0.02; effect size < 0.31; Table S1).

In addition to amplitude, we examined the half-width, area, and rise times of supralinear responses during near-simultaneous activation (Figures 3J, S6G, and S6H). Half-width and area of the supralinear voltage responses were consistently longer in IT neurons than ET neurons (regardless of proximal branch type; Figure 3J), consistent with differences in the membrane properties (Figure S1). However, the rates of rise in IT versus ET basal dendrites were not significantly different (Figure S6G). This contrasted with our observation that, during continuous spine stimulation, the dV/dt of the supralinear responses were significantly slower in IT basal dendrites (Figures 2E and 2F). This discrepancy suggested that near-simultaneous stimulation of dendritic spines failed to account for key differences in the voltage response during our continuous stimulation paradigms.

Supralinear response sensitivity to interspine stimulation rates

The mean total stimulation rates (80–500 Hz; Figures 1, 2, and S3–S5) during continuous spine stimulation never approached interspine stimulation rates utilized when each spine was targeted only once (2 kHz; Figures 3 and S6). We therefore modified our simple stimulus paradigm to include a range of interspine stimulus rates of a fixed number of spines (100–2,000 Hz; Figure 4A; see STAR Methods). Minimal stimulation rates (e.g., interspine stimulus interval of 10 ms, 100 Hz) evoked responses equivalent to the linear sum, and increasing this stimulus rate (at a fixed number of spines) evoked supralinear responses (Figure 4B). The rate sensitivity of the response depended on neuron and compartment type. In IT basal and apical oblique dendrites, as well as the ET apical obliques, response amplitudes increased gradually with rate (Figure 4B). In contrast, ET basal dendrites exclusively exhibited a sharp increase in the amplitude at a particular input rate, which then saturated. This saturation accounted for why ET basal dendrites during continuous spine stimulation had exhibited all-or-none responses at rates far below near synchrony (Figures 1 and 2).

To quantify rate sensitivity, we fit sigmoid curves to the normalized amplitude of the supralinear responses from these experiments (Figure 4; STAR Methods). This provided a slope factor (estimating how graded or step-like the changes in the amplitude were as a function of input rate) and the half-maximal rate (the input rate at which the supralinear response was half the maximum measured). Half-maximal rates varied widely from dendrite to dendrite, and did not depend upon compartment or neuron type (Figure 4C). However, the slope factors were significantly lower in ET basal dendrites (Figure 4D; IT basal: 182.34 ± 28.45 Hz, n = 25; IT apical oblique: 172.50 ± 48.76 Hz, n = 9; ET basal: 42.97 ± 8.95 Hz, n = 18; ET apical oblique: 279.23 ± 45.69 Hz, n = 17). Step-like rate sensitivity was not unique to ET basal dendrites (Figure 4E), but unlike other compartments, ET basal dendrites exclusively exhibited low slope factors, suggesting that this compartment type was particularly sensitive to input rate. Thus, on average, the rate sensitivity depended on the neuron subtype (i.e., ET basal versus IT basal) and also the subcompartment (i.e., ET basal versus ET apical oblique).

We next examined some factors that could contribute to the variability in the rate sensitivity among dendrites. Step-like rate sensitivity of ET basal dendrites was not the result of voltagegated sodium channels (control slope factor: 3.3 ± 2.2 Hz; slope factor in 1 mM

TTX: 3.8 ± 2.7 Hz; n = 3). Also, somatic input resistance did not correlate with slope factor ($r^2 = 0.08757$) since ET neurons (which have a lower somatic input resistance) possessed apical oblique dendrites with shallow rate sensitivity. We also analyzed how the spatial location of the stimulated spines within the dendritic branch might contribute to the slope factor and half-maximal rate (Figures S7A–S7E). While the spatial distribution of targeted spines did not account for branch-type differences in rate sensitivity (Figure S7F), slope factor correlated with the location of the targeted spines in ET neurons (Figure S7B) but not IT neurons (Figure S7D). Similarly, the half-maximal rate of ET basal dendrites (but not ET apical obliques; Figure S7C) was reduced if the targeted spines were closer to the tip of the branch. Differences were not due to the amplitude, rise time, and half-width of individual EPSPs (Figure S7G–S7I). Combined, these data suggested that differences in the local impedance along the length of the branch (Branco and Häusser, 2011; Branco et al., 2010) contribute to rate sensitivity in ET dendrites more than IT dendrites.

Elevations in the input rate during continuous-spine-stimulation-triggered supralinear events

During protocols in which each spine was stimulated once, the amplitude of the dendritic response depended on the interspine stimulus rates (Figure 4). We therefore tested how rate contributed during continuous spine stimulation. For these experiments, we focused upon ET dendrites in which the supralinear excursions were most clearly discernible as discrete events (nine ET basal and one ET apical oblique dendrite, n = 10 total). From moment to moment, during continuous spine stimulation, at least two factors varied: (1) temporal clustering and/or (2) spatial clustering of the targeted spines. We estimated each of these factors with a continuous function to capture how they changed in time (for details see STAR Methods; Figure 5), then calculated event-triggered averages (ETAs) for each of these estimates 200 ms before and 50 ms after the start of supralinear events (Figures 5B–5E).

The continuous input rate was significantly elevated prior to each event compared with random time triggered averages (RTAs). In seven out of ten dendrites tested, the peak of the ETA was greater than the standard deviation of the RTA. Rate was consistently elevated prior to supralinear events, and the peak of the ETA of continuous input rate increased to $159.8\% \pm 6\%$ of the RTA (n = 10 dendrites). By contrast, spatial clustering did not change prior to events. The ETA of the mean path distance never fluctuated beyond the standard deviation of the RTA (0/10 dendrites) and no decrease in the mean path distance ETA was observed (Figure 5E). These data indicated that, when spines are repeatedly driven independently by Poisson-based stimuli, the input rate along the branch was the key contributor, not spatial clustering. These data do not preclude the possibility that, in other stimulation paradigms in which stronger spatial clustering was introduced (not tested here), stronger reductions in the mean path distance could also drive supralinear events. In ET dendrites, rate sensitivity correlates with location along the dendritic branch (Figure S7), suggesting that it is possible that direction selectivity previously observed during simpler stimulus paradigms (Branco et al., 2010) could also occur during continuous spine stimulation.

Rate sensitivity curves account for the difference between dendrites in the voltage response to continuous spine stimulation

Input rate was a key factor in driving supralinear events (Figure 5), so we tested whether rate sensitivity curves could inform/predict how dendrites responded during continuous spine stimulation. We calculated the rate sensitivity curve from stimulating a fixed number of spines (each spine only once) across a range of interspine intervals (as in Figure 4), and then tested how the same dendrite responded to different levels of continuous spine stimulation (Figure 6). To capture the distribution of input rates during the continuous spine stimulation regime, we made histograms of the peaks in the continuous input rate function for each trial (calculated as described in Figure 5 and STAR Methods). The rate sensitivity curves were predictive of which continuous spine stimulation trials exhibited supralinear excursions. Continuous stimulation trials without supralinear excursions had inputs rates below the amount necessary according to the rate sensitivity curves (22/25 trials for 11 dendrites), whereas those with supralinear excursions had a subset of input rates sufficient to drive supralinearity on the rate sensitivity curves (18/24 trials for 7 dendrites). Next, we tested how the slope factor from the rate sensitivity curves related to the structure of the voltage responses during continuous spine stimulation (i.e., Figure 2I). Branches with steep slope factors (>100 Hz) exhibited all-or-none, stereotyped voltage excursions during continuous spine stimulation (Figure 6A), which in turn resulted in voltage distributions with two peaks (Figures 6C and 6D). Branches with shallow slope factors exhibited supralinear voltage excursions that were variable (Figure 6B), resulting in broader voltage distributions around a single peak (Figures 6C and 6D). Slope factor was predictive of the supralinear response during continuous spine stimulation regardless of dendrite or neuron type. Thus, an ET apical oblique with a steep rate sensitivity curve (e.g., Figure 6A) exhibited step-like responses and two peaks in the distribution of voltages during continuous spine stimulation. Together, these data suggest that the rate sensitivity is the key parameter for extrapolating continuous stimulation responses from fixed interval spine stimulation protocols.

Rate sensitivity shapes how dendrites respond to network oscillations

Neocortical networks, and the primary motor cortex in particular, exhibit strong oscillatory properties during several behavioral states (Castro-Alamancos, 2013; Davis et al., 2012; Fisher et al., 2016; Neske, 2016). To examine how rate-dependent boosting in the dendrites shapes a neuron's response to oscillations in network activity, we developed a simple model of input rate to output voltage (Figure 7A) using the experimentally derived rate sensitivity curves (Figure 4). These models responded in similar manner (Figures 7B–7D) to what we had observed experimentally (Figures 2 and 6), further suggesting that the rate sensitivity was sufficient to account for the differences across dendrite types.

We then tested how the simple models responded when the mean input rate changed with time. Stimulus events still occurred randomly, but shared an oscillating mean rate designed to replicate neocortical oscillations observed *in vivo* (12 ± 4 Hz, on a 7 Hz carrier frequency; Figures 7E–7G). All three models exhibited some voltage oscillations in phase with the oscillations of input rate, but the gain of this voltage response was larger in the supralinear models. This was largest in the model with steep rate sensitivity (Figure 7G).

The strength in voltage oscillation caused by supralinear boosting depended on the carrier frequency (Figure 7H). Low carrier frequency oscillations (1–10 Hz) were enhanced, whereas high carrier frequency oscillations (i.e., 100 Hz) were not. This was because at higher carrier frequencies the in-phase oscillation amplitudes were limited by the time course of experimentally measured ETAs (Figure 5). These results predict that dendrites will preferentially enhance the subthreshold voltage gain for lower-frequency network oscillations (i.e., theta and delta) over faster ones.

Since our experimentally measured rate sensitivity curves suggested that the half-maximal rates varied greatly from dendrite to dendrite, we also systematically shifted the half-maximal rates in both models (Figures 7I, 7J, and S8). Even subtle oscillations (± 1 Hz) in the mean input rate drove oscillations of several millivolts in the supralinear output from the steep model (Figure 7J). The gain of the voltage oscillation in response to oscillating inputs in the steep model depended on the difference between the half-maximal rate and the mean rate of the inputs. While the gain increase was weaker in the shallow model, it contributed equivalently over a wider range of half-maximal rates. Combined, these results suggested that steep rate sensitivity may provide a multiplicative increase in the gain of the voltage response.

DISCUSSION

In this study we tested how the proximal dendrites of two distinct categories of L5 pyramidal neurons integrate input designed to mimic a continuously active network. Under these stimulus conditions, dendritic boosting could be reliably triggered by modest elevations in the total input rate of uncorrelated inputs distributed along a dendritic branch. We conclude that near-simultaneous spine activation of spatially clustered spines is not a prerequisite for dendritic boosting. This is consistent with anatomical studies demonstrating that afferent inputs carrying matched signals (e.g., matched orientation receptive fields) can be clustered (Iacaruso et al., 2017; Lee et al., 2016a; Scholl et al., 2017), but also can be distributed along dendritic branches (Lee et al., 2016b; Scholl et al., 2021). Similarly, isolated dendritic events in awake, behaving animals can be highly local (<10 μm) or branch-wide (Cichon and Gan, 2015; Hill et al., 2013; Kerlin et al., 2019; Lavzin et al., 2012; Takahashi et al., 2012).

Our data suggest that dendrites respond to selective features of the spatiotemporally complex inputs they receive. Repeated trials with the same frozen spatiotemporal pattern of stimulation to a dendritic branch elicited similar voltage responses (Figures 1 and S4) that were reminiscent (albeit with less sharp temporal resolution) of how neurons reliably fire action potentials at precise times when driven by frozen noise currents (Mainen and Sejnowski, 1995). While proximal dendrites amplify high rates of combined input, the dendritic boosting was limited by the window of integration of the dendrite. Thus, the gain of the response to lower-frequency oscillations (<10 Hz) typical during slow wave, theta, and delta rhythms was preferentially amplified. It is possible that, with different (i.e., suprathreshold driving) regimes, faster fluctuations in input could also be amplified, as we and others have observed previously using point current injections at the soma (Higgs and Spain, 2009, 2011; Kalmbach et al., 2017). Our model also does not include the somatic frequency selectivity that ET and IT neurons can possess both subthreshold

(Dembrow et al., 2010, 2015) and suprathreshold (Newkirk et al., 2021). Nevertheless, our findings are consistent with findings that L5 neurons contribute to reinforcing low-frequency oscillations (Beltramo et al., 2013; Castro-Alamancos, 2013; Stern et al., 1997; Vesuna et al., 2020), initiating up states (e.g., during slow wave sleep [Neske, 2016; Seibt et al., 2017]) and initiate and propagate neocortical epileptic seizure discharges (Hoffman et al., 1994; Ping and Jin, 2016). The sharp rate sensitivity of ET basal dendrites renders them particularly sensitive to subtle low-frequency input oscillations. This arrangement has strong consequences for spreading slow oscillations as ET neurons are a primary output from neocortex to downstream structures.

Differences in dendritic integration that we observe here between neuron types are consistent with a growing body of evidence that the temporal window of integration differs between ET and IT dendrites (Dembrow et al., 2015; Grewe, 2010; Kalmbach et al., 2015, 2017; Krieger et al., 2017). Surprisingly, we also find that, within ET neurons, the basal and apical oblique dendrites also exhibit different rate sensitivities (Figure 4). Several possible mechanisms may contribute to step-like sensitivity in ET basal dendrites. The composition of NMDA receptors, critical for shaping supralinear integration (Major et al., 2008, 2013), varies depending upon the afferent input type (Kumar and Huguenard, 2003; Miyata and Imoto, 2006). Which afferent inputs preferentially target ET basal dendrites remains incompletely defined; however, it is notable that their deeper laminar location (Figure S1) may provide them with a distinct complement of thalamic and cortical inputs (Hooks et al., 2013; Kawaguchi, 2017; Mao et al., 2011; Petreanu et al., 2009; Rah et al., 2013; Shigematsu et al., 2016). In particular, basal dendrites receive a large proportion of the recurrent excitatory connections within L5 (e.g., Frick et al., 2008; Markram et al., 1997).

The functional roles of L5 proximal apical oblique and basal dendrites remain elusive in awake, behaving animals. Both proximal compartments exhibit strong increases in calcium during anesthesia-induced up states, even in the absence of somatic/axonal firing (Hill et al., 2013) and exhibit robust calcium fluctuations during paroxysmal depolarizing shifts in *ex vivo* slices (Schiller, 2002). Our data suggest supralinear integration may make proximal branches able to detect moments of elevation in local network activity and/or ascending feedforward thalamic afferents. This arrangement requires that afferent inputs targeting different branches be somewhat correlated or the supralinear events in different dendritic branches will be poorly matched in time. Our data suggest, that with the presence of even subtle network-level oscillations of the afferent inputs, supralinear events in separate proximal branches would be in phase and thus summate. This endows dendrites with the ability to encode moments of sparse, synchronous activation as well as shared moments of collective elevation in the rate of inputs across multiple dendrites. These results provide a key insight into how dendritic integration may control gain during continuous activity in a manner sensitive to network state.

Limitations of the study

The glutamate uncaging approach used in this study mimicked ongoing input with precise spatiotemporal control not possible when injecting currents/conductances at a single point along a dendrite (Dembrow et al., 2015; Fletcher and Williams, 2019; Harnett et al.,

2013; Kalmbach et al., 2017; Oviedo and Reyes, 2012), and permitted examination of integration in small-caliber dendrites that are difficult to reliably record from (Nevian et al., 2007). Nevertheless, important caveats must be considered when extrapolating how these data replicate dendritic integration *in situ*. First, both the divisive and subtractive effects of inhibition (Gidon and Segev, 2012; Jadi et al., 2012) are likely to shape dendritic processing during continuous spine stimulation. Second, although we made efforts to match the single-spine gluEPSPs to those triggered by endogenous release (Figure S2; Table S1), our stimulation targets may not precisely match the postsynaptic density for all spines targeted. Although some of recruitment of extrasynaptic glutamate receptors is known to occur with endogenous release (Chalifoux and Carter, 2011), we cannot account for how much extrasynaptic activation occurred with our stimulation. Third, directly stimulating dendritic spines necessarily bypassed presynaptic contributions to how the input activity is encoded. Changes in release probability from short-term depression or facilitation vary greatly depending upon the pre- and post-neuron identity and recording condition (Borst, 2010; Markram et al., 1997, 1998; Schiller et al., 2000; Wang et al., 2006). Short-term depression also provides dynamic gain control, suppressing the influence of presynaptic neurons firing at high rates relative to those firing at low rates (Abbott et al., 1997; Rothman et al., 2009). Interestingly, we find the opposite arrangement with supralinear dendritic integration at the postsynaptic side, wherein high input rates are preferentially boosted making postsynaptic neurons particularly responsive to slow oscillations in input.

STAR★METHODS

RESOURCE AVAILABILITY

Lead contact—Further information and requests for resources related to this article should be directed to and will be fulfilled by the Lead Contact, William J. Spain (spain@uw.edu).

Materials availability—This study did not generate new unique agents.

Data and code availability

- All experimental and modeling data reported in this paper will be shared by the lead contact (William J. Spain, spain@uw.edu) upon reasonable request.

- Original code for the simple input rate model has been deposited at https://zenodo.org/record/5895134#.Yfr4mvXMKF0 and is publicly available as of the date of publication.

- Any additional information required to reanalyze the data reported in this paper is available from the lead contact, William J. Spain (spain@uw.edu) upon reasonable request.

EXPERIMENTAL MODEL AND SUBJECT DETAILS

Animals—All experiments were performed in accordance with institutional and national guidelines for animal care approved by the Institutional Animal Care and Use Committee at the University of Washington. Male and female mice from the following transgenic lines: *Thy1h*-eyfp (B6.Cg-Tg(*Thy1*-EYFP)-HJrs/J, RRID:IMSR_JAX:003782), and *Etv1*-egfp

Tg(*Etv1*-EGFP)-BZ192Gsat/Mmucd, RRID:MMRRC_011152-UCD were utilized. Etv1 mice maintained with the outbred Charles River Swiss Webster background (Crl:CFW(SW, RRID:IMSR_CRL:024).

METHOD DETAILS

Tissue preparation—Mouse primary motor cortex was obtained from 4 to 16 weeks old male and female Thy1-h and Etv1 mice were deeply anesthetized by IP administration of ketamine (130 mg/kg) and xylazine (8.8 mg/kg) mix and were perfused through the heart with chilled ($2–4°C$) sodium-free aCSF consisting of (in mM): 210 Sucrose, 7 d-glucose, 25 $NaHCO_3$, 2.5 KCl, 1.25 NaH_2PO_4, 7 $MgCl_2$, 0.5 $CaCl_2$,1.3 Na-ascorbate, 3 Na-pyruvate bubbled with carbogen (95% O_2/5% CO_2). Off-coronal slices ($15°$ tilted rostrally) 300 mm thick were generated using a Leica vibratome (VT1200, Leica, Germany) in the same sodium-free aCSF and were transferred to warmed ($35°$) holding solution (in mM): 125 NaCl, 2.5 KCl, 1.25 NaH_2PO_4, 26 $NaHCO_3$, 2 $CaCl_2$, 2 MgCl2, 17 dextrose, and 1.3 sodium pyruvate bubbled with carbogen (95% O_2/5% CO_2). After 30 min of recovery, the chamber holding slices was allowed to cool to room temperature.

Surgeries—For a subset of experiments, Etv1 mice (4–8 weeks of age), neurons in L5 of motor cortex were retrogradely labeled to determine long-term projection target. Mice were anaesthetized with isoflurane (1–4% mixed with oxygen), prepped for surgery with shaving of the surgical site, opthalamic ointment to the eyes and injection of local analgesic (subcutaneous Meloxicam, 5 mg/kg). Once placed in a stereotaxic apparatus, the surgical site was cleaned with betadine scrub and the animal was draped. After a midline incision, skull cleaning and drying, craniotomies were made over the injection target with a dental drill. Over the location of injection site, a small incision in the dura was made. Injections were performed using a pulled glass pipette (20–35 μm diameter tip) mounted on a Nanoject II small volume injector (Drummond Scientific, Broomall, PA). Red fluorescent-labeled microspheres (Lumafluor, Durham, NC) were injected into either the pons (3 mice; 4.2 mm posterior, 0.8 mm lateral, 5.4 mm ventral to Bregma, 2–3 injections in same location 69 nL each) to retrogradely label corticopontine and the contralateral cortex (2 mice; 2 injections of 69 nL: 1.0 mm anterior, 1.5 mm lateral, and 1.4 mm ventral from Bregma) or (2 mice; 2 injections of 69 nL: 1.0 mm anterior, 1.5 mm lateral, and 3.0 mm ventral from Bregma, 2 injections, 69 nL each) to label commissural IT neurons. Each individual injection was performed at a speed of 23 nL/s, separated by 30 s to 2 min interval. For all injections, the pipette was left in place for 2–5 min before removing it from the brain. The craniotomy was closed using Kwik-Sil (WPI, Germany), and the wound sutured. Mice were monitored daily to ensure complete recovery and given analgesics (Meloxicam, 5 mg/kg) as needed. Retrograde tracer was given > 5 days after surgery to allow sufficient labeling of pyramidal neurons in the motor cortex before euthanatizing mice and collecting tissue for recordings.

Recordings—*Ex-vivo* recordings were made in aCSF: (in mM): 125 NaCl, 3.0 KCl, 1.25 NaH_2PO_4, 26 $NaHCO_3$, 2 $CaCl_2$, 1 MgCl2, 17 dextrose, and 1.3 sodium pyruvate bubbled with carbogen (95% O_2/5% CO_2) at $32–35°$, with synaptic inhibition blocked using 100 μM picrotoxin. Layer 5 pyramidal neurons in the motor cortex expressing eYFP or eGFP were targeted for somatic recording using two photon (2P) microscopy combined with Dodt

optics by performing whole-cell patch recordings with pulled borosilicate glass pipettes (P1000, Sutter, Novato, CA) with tip openings about 1 μm and resistances of 4–6 MΩ following coating of the taper with heat-cured Sylgard (Dow Corning, Midland, MI) to reduce capacitance. Recording pipettes were filled with an internal solution containing (in mM): 140 K-gluconate, 14 KCl, 10 HEPES, 4 MgATP, 0.3 NaGTP, 7 2K-phosphocreatine, and 4 2Na-phosphocreatine (pH 7.42 with KOH) with Neurobiotin (0.1–0.2%), Alexa 594 (A594, 40 μM, Molecular Probes, ThermoFisher Scientific). For all experiments except for those measuring endogenous EPSPs by puffing hypertonic solution (see below), Oregon Green BAPTA-6F (OGB6F, 100 μM, Molecular Probes, ThermoFisher Scientific) was also included in the internal recording solution. This low-affinity calcium indicator was included to monitor baseline calcium levels in the dendrite (as an indicator of dendrite health and stability) were unchanged between stimulus trials. Current clamp recordings were performed using an Axoclamp 2B amplifier (Molecular Devices, Sunnyvale, CA, USA) in bridge balance mode with 10 kHz low-pass filtering and 20 kHz data sampling through an ITC-18 digital board (HEKA, Lambrecht, Germany) and controlled using custom protocols written in Igor Pro (Wavemetrics, OR). Reported voltages were corrected for the measured liquid junction potential (8 mV) and recordings with >25 MΩ series resistance or <0 mV spike overshoot were discarded.

2-Photon imaging and glutamate uncaging—Precise focal activation of individual dendritic spines was performed using 2P laser activation guided by a dual-galvanometer based scanning system (Ultima In Vitro Multiphoton Microscope System, RRID: SCR_017142) from Bruker Technologies (Middleton, WI). Ultra-fast pulsed laser light (Chameleon Ultra II; Coherent; Santa Clara, CA) at 810 nm was used to excite A594 and OGB6F, guided by galvanometer-controlled (6 mm, Cambridge Technology, Bedford, MA) mirrors through a 40x objective on a Zeiss microscope. Reflected fluorescent light was separated using two dichroic mirrors and through green (ET525/70m-2P) and red (ET650/75m-2P; Chroma, Bellow Falls, VT) emission filters and collected using gallium arsenide phosphide (GaAsP) detectors. To photolyze caged glutamate, a second laser (Chameleon Ultra II; Coherent, Palo Alto, CA) set to 720 nm was guided by a separate set of galvanometer-controlled mirrors (3 mm, Cambridge) into the light path. The intensity of each laser beam reaching the sample was independently attenuated using an elecro-optical modulator (Pockels cell, Conoptics, Danbury CT), and additionally the uncaging light passed through a custom made passive 8x pulse splitter to reduce photodamage (Ji et al., 2008). 4-Methoxy-7-nitroindolinylcaged-L-glutamate (MNI-glutamate, 3–4 mM; Tocris, Bio-Techne, Minneapolis, MN) was bath applied, recirculated using an oxygenated reservoir (5 mL). Prairie View and TriggerSync (v2.0.5) software in conjunction with custom-written acquisition code in Matlab (version R2012b, Mathworks, Natick, MA) was utilized to control laser intensity, the galvonometer-controlled beam location within the field of view, and to collect imaging, stimulation parameters, and electrophysiological data.

When targeting spines along a dendritic branch, experiments were restricted to regions of the proximal dendrites with spines that were constrained within several mm in depth. Targeted proximal apical obliques were connected to the apical trunk < 50 μm from the soma. The absolute distances from the soma to the centroid of our stimulation range were comparable

across compartments (mean distance in μm ± SD: IT basal, 99.9 ± 39.9, n = 29; IT a.o. 106.7 ± 33.4, n = 17; ET basal, 90.7± 32.7, n = 41; ET a.o., 112.6 ± 33.4, n = 25). On average targeted basal locations were closer to the soma than apical obliques but this did not quite rise to significance (2-way ANOVA $F_{(1,108)}$ < 3.762, p > 0.06; Tukey's multiple comparisons were all p > 0.09). The span of the dendritic branch containing spines targeted for stimulation was on average 62.4 μm ± 17.4 SD (n = 112). The spans of dendrites targeted did depend upon compartment type, but not cell type (span ± SD in μm; IT basal, 62.7 ± 17.1, n = 29; IT a.o. 55.7 ± 19.9, n = 17; ET basal, 67.8 ± 18.1, n = 41; ET a.o., 57.7 ± 11.9, n = 25; 2-way ANOVA, $F_{(1,108)}$ = 6.387, p = 0.0129 vs. $F_{(1,108)}$ = 1.116, p = 0.29). To roughly estimate the density of spines for each compartment type we counted the total number of spine-like protrusions from high resolution 2-photon z-stacks of a subset of dendrites stimulated using glutamate uncaging (8 per compartment type). Spine densities using this method were calculated as less than 1 spine per mm (spines/μm ± SD: IT basal, 0.892 ± 0.125; IT a.o. 0.740 ± 0.138; ET basal, 0.772 ± 0.154; ET a.o., 0.822 ± 0.075; n = 8 each compartment type; 2-way ANOVA, interaction: $F_{(1,28)}$ = 5.076, p = 0.03; cell type: $F_{(1,28)}$ =.19, p = 0.67; compartment type: $F_{(1,28)}$ = 1.3, p =.26; Tukey's multiple comparisons: p > 0.1).

Several steps were taken to maximize our ability to reliably mimic synaptic input in our glutamate uncaging experiments. First, in a separate set of controls, we measured the size of endogenous EPSPs onto the ET and IT proximal dendrites (Figure S2, Table S1, and Video S1). To drive exocytosis from endogenous presynaptic terminals synapsing onto these dendrites, we focally extruded hypertonic solution (HEPES buffered ACSF, 300 mM sucrose, 1 μM TTX and 5 μM Alexa 488) from a patch pipette (4–6 MΩ) with positive pressure (1–4 PSI for 2 seconds via a Picospritzer II, General Valve, Fairfield, NJ). Location and intensity of the patch electrode puff was adjusted to ensure coverage over a single dendritic location proximal to the dendrite while recording endogenous EPSPs measured from the somatic electrode. A time series of 2-photon images were captured to monitor the size of the extruded hypertonic solution by the spread of Alexa 488 dye (Video S1). Location and brief exposure times (0.2 ms) of laser intensity were chosen to best match amplitude, half-width and rise time of the sucrose-evoked EPSPs (Figure S2 and Table S1). Photolysis targets were placed adjacent (~ 0.5 – 1 μm) to the spine head. Target locations were chosen to match average sucrose-evoked responses. When selecting spines to stimulate with glutamate uncaging along the dendritic branch, effort was made to only target spines with the head within a micron of the 2-photon imaging plane, slightly broader than the 2-photon imaging plane (0.4–0.8 μm) shown in images. Single spine responses were stable, but gluEPSPs varied greatly from spine to spine. It is possible that some spines may experience lower levels of glutamate in cases where the post synaptic density of the spine was not precisely directly adjacent to our target stimulation. In a separate set of control experiments (Figure S2C) we confirmed that targets further (> 1.4 μm) from the spine head did not evoke visible single spine responses, indicating that the cloud of glutamate caused by photolysis was focal. When picking spines to target, attempts were made to avoid adjacent targets below this resolution. Photolysis was also tested in the absence of glutamate to ensure that the 2P laser light alone had no discernible effect. Galvonometer control was confirmed by daily calibration by photolyzing a target grid covering the field of view onto

an ink-coated coverslip. To confirm and correct for any movement in x, y or z axes, three z-plane images were taken (0.5 μm steps) between at least every other trial and the stage was adjusted using custom-written algorithms in Matlab that analyzed the image for comparison for movement compared to a stored initial reference image with feed back to the motorized stage (x,y) and objective (z). To minimize the chances of any spine plasticity during our stimulus protocols we chose stimulation paradigms that rarely evoked action potentials, with trials % 3 s long, and that were separated by 30–60 s intervals. We did not observe changes in spine morphology at the resolution of our image collection, nor changes in the gluEPSP amplitudes (data not shown) from our stimulation protocols.

For all glutamate uncaging experiments, targeted spines were activated in a random spatial sequence. All experiments testing ranges of spine counts and/or interspine intervals had the order of the stimulus conditions randomized. For the interspine rate interval trials designed to generate the rate sensitivity curves, the number of spines was typically 9 above the minimum necessary to drive a supralinear response when activated near-simultaneously. The range of spines used across different dendritic compartments was similar (25 IT basal dendrites with a range of 19–35 spines; 9 IT apical oblique dendrites with a range of 21–35 spines; 18 ET basal dendrites with a range of 23–38 spines; 17 ET apical oblique dendrites with a range of 21–37 spines), and there was no significant difference in the spine counts used across types (2-factor ANOVA, $F_{(1,65)} < 2.6$, $p > 0.1$ for all factors).

For continuous spine stimulation regimes, Poisson distributed stimulation times were generated in Matlab using custom written scripts. For each spine, the probability of a stimulus occurring at any sampling point (0.05 ms) was set by a user defined mean rate. Two constraints were imposed upon the randomness of these stimulation times. First, to make the Poisson distribution of stimulation times more like the firing pattern of a neuron, we imposed a refractory period by removing any stimuli 2 ms after each stimulation time. Second, our apparatus required a minimum interspine stimulus interval of 0.5 ms (0.2 ms light dwell time with light on, 0.2 ms minimal time to change position with light off). We thus shifted each stimulus train in time such that any interspine intervals less than 0.5 ms were adjusted to 0.5 ms. All continuous stimulation rates reported are the actual rate after these constraints were applied. In experiments where patterns of continuous spine stimulation were frozen, both the spatial and the temporal stimulation patterns were fixed. For a subset of uncaging experiments (Figure S6), D-L-2-Amino-5-phosphonopentanoic Acid (APV, 100 μM, Tocris), and tetrodotoxin (TTX, 1 μM, Tocris) was utilized to identify active conductances that contribute to supralinear responses.

Analytical model—For the simple analytical model of voltage based upon input rate, inhomogeneous Poisson-like spike trains for 60 inputs were generated by the same custom written script in Matlab as described above, except the mean rate from which the Poisson distribution was centered was set by a sine wave with a user defined carrier frequency, mean rate, and amplitude of oscillation and minimum interspine stimulus interval was no longer constrained to be R 0.5 ms. For each condition, 50 seconds of input events was generated, except when different carrier frequencies were tested. For comparing the voltage oscillations caused by different carrier frequencies (Figure 7H), each frequency was tested for a duration that drove 300 cycles of oscillation, to provide comparable resolution. These trains were

then transformed into voltage signals using a custom written analytical model in IgorPro. The trains were collapsed into a single event train, convolved with a smoothed and reversed ETA (calculated in Figure 5) to make a continuous estimate of rate. The voltage response was calculated as function of the rate (x) in Hz using either a linear function:

$$V_{linear} = 0.002x,$$ (Equation 1)

or a sigmoid function:

$$V_{sigmoid} = \frac{12}{1 + e^{\left(\frac{HR - x}{slope}\right)}} + 0.002x$$ (Equation 2)

The sigmoid was set as shallow ($slope = 250$ Hz) or steep ($slope = 25$ Hz) and a half maximal rate (HR) that was set to 560, 760, 960 or 1160 Hz.

QUANTIFICATION AND STATISTICAL ANALYSIS

Statistics—For all statistical comparisons between multiple groups across different factors, 2-factor analysis of variance was used, with Tukey's multiple comparisons to directly compare between groups in Prism 8 (GraphPad, San Diego CA). For comparisons between two groups, t-tests, Kolmogorov-Smirnov, or Wilcoxon Rank Sum tests (depending upon how the data were distributed) and Effect Size calculations were performed in IgorPro. Box plots shown indicate the minimum, lower quartile, median, upper quartile, and maximum value for each distribution. Linear correlation coefficients were calculated in IgorPro, with the p values calculated testing the null hypothesis that the correlation coefficient is zero (two-tailed).

Quantification—Uncaging and electrophysiological data were analyzed using custom-written analysis packages in Igor Pro 6.37 (Wavemetrics, Lake Oswego, OR). Individual spine responses that were collected by stimulating individual spines 200 ms apart were used to calculate the linear sum. Sucrose-evoked EPSPs were identified and collected using custom code adapted from Mini Analysis code by Aaron Milstein. The half-widths, amplitudes 20–80 rise times were calculated from both sucrose and uncaging-evoked responses using this code as well. Photomicrographs shown are from the maximum projection of 1 mm z-stacks processed in ImageJ (Schindelin et al., 2012).

The linear sum for both continuous and fixed interval trials were calculated by summating the individual 2P-glu evoked waveforms offset in time at intervals according to the stimulation times. Rise time was calculated as the time from 10 to 90% of the peak response, and half-width the time of the voltage excursion above ½ the maximum amplitude. In a subset of the fixed interval and continuous trials, the evoked depolarization was sufficient to drive action potentials (e.g. Figure S4). All trials with firing were excluded from subsequent analysis. Phase plots of the voltage response during the continuous spine stimulation regimes were calculated as follows. The voltage response during stimulation was baseline subtracted, filtered using a sliding average window 2.5 ms in width, and plotted against its calculated first derivative (dV/dt).

Histograms of the distribution of voltages for ET and IT basal dendrites were calculated by first determining whether the trial exhibited a voltage response peak 0.5 mV greater than the expected linear sum. The voltage response during stimulation was then normalized by subtracting the baseline and dividing by the maximal response. The distribution of normalized voltages was then binned (20 bins with 0.05 width from 0 to 1) and normalized to the total number of counts to plot the probability density for each bin.

To calculate the rate sensitivity curves (Figures 4 and 6), the linear sum at each rate tested was calculated and subtracted from the evoked response. This subtracted curve was then normalized such that the minimum response was zero and the maximal response was set to one. A sigmoid was fitted to the response using the following equation:

$$Normalized\ V_m = \left(\frac{1}{1 + e^{\left(\frac{HR - x}{slope}\right)}}\right)$$

(Equation 3)

where *HR* is the half maximal rate and *slope* is the slope factor (the steepness of the sigmoid). To facilitate comparisons in the slope factor as shown in Figure 4D, rate-sensitivity curves were further normalized in the x axis by subtracting the half maximal rate from all rate values.

The continuous input rate function was calculated by collapsing stimulation times from all activated spines into a single train. This combined stimulus train was then convolved with a 1 ms wide step function to generate a continuous function of the combined input rate. A 1 ms kernel was chosen to minimize any temporal filtering in the analysis that could occur. Similar results were obtained using 1, 10 and 25 ms alpha functions (data not shown). To identify spatial clustering during continuous stimulation, we calculated the minimum distance along the dendrite from each spine targeted for stimulation to every other targeted spine within the last 25 ms. We did not observe reductions in mean path distance (indicating high spatial clustering) at any of the temporal windows tested (1, 10, 25, 50 ms, data not shown). To generate a path along the dendrite, custom software using Matlab Image Processing toolbox commands first rendered the 2P-fluorescent image binary with a user defined threshold to mark pixels within the image as part of the dendrite or not. The shortest path through these identified pixels between each of the marked spine heads was then calculated. After visual confirmation by the user that these image paths traveled along the dendrite length, a distance matrix of these paths (converted into mm) was then used to calculate the characteristic path length in mm for a given set of spines within the 25 ms prior to each stimulation. To facilitate comparison across ET dendrites exposed to a range of stimulation conditions (mean rate per spine from 3 to 10 Hz/spine; 15–43 spines stimulated for each dendrite; mean combined input rates from 110 to 364 Hz per dendrite), the ETA and RTAs for the combined input rate and mean path distance were normalized by dividing by the average of the RTA and multiplying them by 100.

To generate event-triggered averages (ETA), event times were extracted by detecting the start times of supralinear voltage events during continuous stimulation trials. Events were first detected based on the following criteria: the derivative of the voltage trace (which was filtered by Boxcar averaging using a 2.5 ms window) surpassed 0.20 mV/ms and voltage

reached at least 70% of the maximal voltage excursion in the trial. Start time of each supralinear event was identified as the moment when the 70% threshold was passed. For each event input parameter, 200 ms prior to and 50 ms after the start time was averaged to generate the ETA. We chose 200 ms prior to the event time as a conservative estimate of the longest duration of time prior to an event that might drive a supralinear response (e.g. 40 spines at 200 Hz), and the 50 ms after to capture the period during which a supralinear event occurs and returns to baseline. To calculate the RTA the stimulus parameters were collected from 100 random times during the stimulus trial and averaged.

To calculate the distribution of rates during continuous stimulation (Figures 5 and S8), we identified and made a histogram from the peaks in the continuous input rate function using the unipolar peak finder algorithm in IgorPro. This software identified any peaks that had a width of >10 ms. Histograms were generated by counting the number of peaks in bins from 10 Hz to 1960 Hz in 50 Hz increments.

Time series of 2P-images collected while whole-cell-patch recording from a ET neuron filled with red Alexa 594 dye (40 μM) and during 2 puffs of hypertonic solution (HEPES buffered ACSF, 300 mM sucrose, 1 μM TTX and 5 μM Alexa 488) from the puffer electrode (green) over a basal dendrite. When hypertonic solution was extruded, the spread of the Alexa 488 dye was localized (30–40 μm in diameter) to the target dendrite. Images were collected at 512×512 with 0.585 μm/pixel, with a frame rate of 1 Hz.

Supplementary Material

Refer to Web version on PubMed Central for supplementary material.

ACKNOWLEDGMENTS

REFERENCES

Abbott LF, Varela JA, Sen K, and Nelson SB (1997). Synaptic depression and cortical gain control. Science 275, 220–224. [PubMed: 8985017]

Aeed F, Shnitzer T, Talmon R, and Schiller Y (2020). Layer- and cell-specific recruitment dynamics during epileptic seizures *in vivo*. Ann. Neurol 87, 97–115. [PubMed: 31657482]

Antic SD, Zhou W-L, Moore AR, Short SM, and Ikonomu KD (2010). The decade of the dendritic NMDA spike. J. Neurosci. Res 88, 2991–3001. [PubMed: 20544831]

Baker A, Kalmbach B, Morishima M, Kim J, Juavinett A, Li N, and Dembrow N (2018). Specialized subpopulations of deep-layer pyramidal neurons in the neocortex: bridging cellular properties to functional consequences. J. Neurosci 38, 5441–5455. [PubMed: 29798890]

Beltramo R, D'Urso G, Dal Maschio M, Farisello P, Bovetti S, Clovis Y, Lassi G, Tucci V, De Pietri Tonelli D, and Fellin T (2013). Layer-specific excitatory circuits differentially control recurrent network dynamics in the neocortex. Nat. Neurosci 16, 227–234. [PubMed: 23313909]

Borst JGG (2010). The low synaptic release probability *in vivo*. Trends Neurosci 33, 259–266. [PubMed: 20371122]

Branco T, and Häusser M (2010). The single dendritic branch as a fundamental functional unit in the nervous system. Curr. Opin. Neurobiol 20, 494–502. [PubMed: 20800473]

Branco T, and Häusser M (2011). Synaptic integration gradients in single cortical pyramidal cell dendrites. Neuron 69, 885–892. [PubMed: 21382549]

Branco T, Clark BA, and Hausser M (2010). Dendritic discrimination of temporal input sequences in cortical neurons. Science 329, 1671–1675. [PubMed: 20705816]

Brette R (2015). Philosophy of the spike: rate-based vs. spike-based theories of the brain. Front. Syst. Neurosci 9, 151. [PubMed: 26617496]

Castro-Alamancos MA (2013). The motor cortex: a network tuned to 7–14 Hz. Front. Neural Circuits 7, 21. [PubMed: 23439785]

Catanese J, and Jaeger D (2021). Premotor ramping of thalamic neuronal activity is modulated by nigral inputs and contributes to control the timing of action release. J. Neurosci 41, 1878–1891. [PubMed: 33446518]

Cauller LJ, Clancy B, and Connors BW (1998). Backward cortical projections to primary somatosensory cortex in rats extend long horizontal axons in layer I. J. Comp. Neurol 390, 297–310. [PubMed: 9453672]

Chalifoux JR, and Carter AG (2011). Glutamate spillover promotes the generation of NMDA spikes. J. Neurosci 31, 16435–16446. [PubMed: 22072693]

Cheney PD, Fetz EE, and Mewes K (1991). Chapter 11. Neural mechanisms underlying corticospinal and rubrospinal control of limb movements. In Progress in Brain Research (Elsevier), pp. 213–252.

Cichon J, and Gan W-B (2015). Branch-specific dendritic Ca^{2+} spikes cause persistent synaptic plasticity. Nature 520, 180–185. [PubMed: 25822789]

Davis NJ, Tomlinson SP, and Morgan HM (2012). The role of beta-frequency neural oscillations in motor control. J. Neurosci 32, 403–404. [PubMed: 22238075]

Dayan P, and Abbott LF (2001). Theoretical Neuroscience: Computational and Mathematical Modeling of Neural Systems (MIT Press).

Dembrow NC, Chitwood RA, and Johnston D (2010). Projection-specific neuromodulation of medial prefrontal cortex neurons. J. Neurosci 30, 16922–16937. [PubMed: 21159963]

Dembrow NC, Zemelman BV, and Johnston D (2015). Temporal dynamics of L5 dendrites in medial prefrontal cortex regulate integration versus coincidence detection of afferent inputs. J. Neurosci 35, 4501–4514. [PubMed: 25788669]

Fisher SP, Cui N, McKillop LE, Gemignani J, Bannerman DM, Oliver PL, Peirson SN, and Vyazovskiy VV (2016). Stereotypic wheel running decreases cortical activity in mice. Nat. Commun 7, 13138. [PubMed: 27748455]

Fletcher LN, and Williams SR (2019). Neocortical topology governs the dendritic integrative capacity of layer 5 pyramidal neurons. Neuron 101, 76–90.e4. [PubMed: 30472076]

Frick A, Feldmeyer D, Helmstaedter M, and Sakmann B (2008). Monosynaptic connections between pairs of L5A pyramidal neurons in columns of juvenile rat somatosensory cortex. Cereb. Cortex 18, 397–406. [PubMed: 17548800]

Gidon A, and Segev I (2012). Principles governing the operation of synaptic inhibition in dendrites. Neuron 75, 330–341. [PubMed: 22841317]

Grewe BF (2010). Back-propagation of physiological action potential output in dendrites of slender-tufted L5A pyramidal neurons. Front. Cell. Neurosci 4, 13. [PubMed: 20508744]

Groh A, Meyer HS, Schmidt EF, Heintz N, Sakmann B, and Krieger P (2010). Cell-type specific properties of pyramidal neurons in neocortex underlying a layout that is modifiable depending on the cortical area. Cereb. Cortex 20, 826–836. [PubMed: 19643810]

Gulledge AT, and Stuart GJ (2003). Action potential initiation and propagation in layer 5 pyramidal neurons of the rat prefrontal cortex: absence of dopamine modulation. J. Neurosci 23, 11363–11372. [PubMed: 14673000]

Harnett MT, Makara JK, Spruston N, Kath WL, and Magee JC (2012). Synaptic amplification by dendritic spines enhances input cooperativity. Nature 491, 599–602. [PubMed: 23103868]

Harnett MT, Xu N-L, Magee JC, and Williams SR (2013). Potassium channels control the interaction between active dendritic integration compartments in layer 5 cortical pyramidal neurons. Neuron 79, 516–529. [PubMed: 23931999]

Harris KD, and Shepherd GMG (2015). The neocortical circuit: themes and variations. Nat. Neurosci 18, 170–181. [PubMed: 25622573]

Hattox AM, and Nelson SB (2007). Layer V neurons in mouse cortex projecting to different targets have distinct physiological properties. J. Neurophysiol 98, 3330–3340. [PubMed: 17898147]

Higgs MH, and Spain WJ (2009). Conditional bursting enhances resonant firing in neocortical layer 2–3 pyramidal neurons. J. Neurosci 29, 1285–1299. [PubMed: 19193876]

Higgs MH, and Spain WJ (2011). Kv1 channels control spike threshold dynamics and spike timing in cortical pyramidal neurones: Kv1 channels control threshold dynamics. J. Physiol 589, 5125–5142. [PubMed: 21911608]

Hill DN, Varga Z, Jia H, Sakmann B, and Konnerth A (2013). Multibranch activity in basal and tuft dendrites during firing of layer 5 cortical neurons *in vivo*. Proc. Natl. Acad. Sci. U S A 110, 13618–13623. [PubMed: 23904480]

Hoffman SN, Salin PA, and Prince DA (1994). Chronic neocortical epilep to genesis *in vitro*. J. Neurophysiol 71, 1762–1773. [PubMed: 8064347]

Hooks BM, Mao T, Gutnisky DA, Yamawaki N, Svoboda K, and Shepherd GMG (2013). Organization of cortical and thalamic input to pyramidal neurons in mouse motor cortex. J. Neurosci 33, 748–760. [PubMed: 23303952]

Iacaruso MF, Gasler IT, and Hofer SB (2017). Synaptic organization of visual space in primary visual cortex. Nature 547, 449–452. [PubMed: 28700575]

Jadi M, Polsky A, Schiller J, and Mel BW (2012). Location-dependent effects of inhibition on local spiking in pyramidal neuron dendrites. PLoS Comput. Biol 8, e1002550. [PubMed: 22719240]

Ji N, Magee JC, and Betzig E (2008). High-speed, low-photodamage nonlinear imaging using passive pulse splitters. Nat. Methods 5, 197–202. [PubMed: 18204458]

Kalmbach BE, Chitwood RA, Dembrow NC, and Johnston D (2013). Dendritic generation of mGluR-mediated slow afterdepolarization in layer 5 neurons of prefrontal cortex. J. Neurosci 33, 13518–13532. [PubMed: 23946410]

Kalmbach BE, Johnston D, and Brager DH (2015). Cell-type specific channelopathies in the prefrontal cortex of the fmr1-/y mouse model of fragile X syndrome. eNeuro 2. 10.1523/ENEURO.0114-15.2015.

Kalmbach BE, Gray R, Johnston D, and Cook EP (2017). Systems-based analysis of dendritic nonlinearities reveals temporal feature extraction in mouse L5 cortical neurons. J. Neurophysiol 117, 2188–2208. [PubMed: 28250154]

Kawaguchi Y (2017). Pyramidal cell subtypes and their synaptic connections in layer 5 of rat frontal cortex. Cereb. Cortex 27, 5755–5771. [PubMed: 29028949]

Kerlin A, Mohar B, Flickinger D, MacLennan BJ, Dean MB, Davis C, Spruston N, and Svoboda K (2019). Functional clustering of dendritic activity during decision-making. eLife 8, e46966. [PubMed: 31663507]

Krieger P, de Kock CPJ, and Frick A (2017). Calcium dynamics in basal dendrites of layer 5A and 5B pyramidal neurons is tuned to the cell-type specific physiological action potential discharge. Front. Cell. Neurosci 11, 194. [PubMed: 28744201]

Kumar SS, and Huguenard JR (2003). Pathway-specific differences in sub-unit composition of synaptic NMDA receptors on pyramidal neurons in neocortex. J. Neurosci 23, 10074–10083. [PubMed: 14602822]

Larkum ME, Nevian T, Sandler M, Polsky A, and Schiller J (2009). Synaptic integration in tuft dendrites of layer 5 pyramidal neurons: a new unifying principle. Science 325, 756–760. [PubMed: 19661433]

Lavzin M, Rapoport S, Polsky A, Garion L, and Schiller J (2012). Nonlinear dendritic processing determines angular tuning of barrel cortex neurons *in vivo*. Nature 490, 397–401. [PubMed: 22940864]

Lee KFH, Soares C, Thivierge J-P, and Béïque J-C (2016a). Correlated synaptic inputs drive dendritic calcium amplification and cooperative plasticity during clustered synapse development. Neuron 89, 784–799. [PubMed: 26853305]

Lee W-CA, Bonin V, Reed M, Graham BJ, Hood G, Glattfelder K, and Reid RC (2016b). Anatomy and function of an excitatory network in the visual cortex. Nature 532, 370–374. [PubMed: 27018655]

Li N, Chen T-W, Guo ZV, Gerfen CR, and Svoboda K (2015). A motor cortex circuit for motor planning and movement. Nature 519, 51–56. [PubMed: 25731172]

Li N, Daie K, Svoboda K, and Druckmann S (2016). Robust neuronal dynamics in premotor cortex during motor planning. Nature 532, 459–464. [PubMed: 27074502]

Llinás R, and Sugimori M (1980). Electrophysiological properties of *in vitro* Purkinje cell dendrites in mammalian cerebellar slices. J. Physiol 305, 197–213. [PubMed: 7441553]

Losonczy A, and Magee JC (2006). Integrative properties of radial oblique dendrites in hippocampal CA1 pyramidal neurons. Neuron 50, 291–307. [PubMed: 16630839]

Losonczy A, Makara JK, and Magee JC (2008). Compartmentalized dendritic plasticity and input feature storage in neurons. Nature 452, 436–441. [PubMed: 18368112]

Mainen Z, and Sejnowski T (1995). Reliability of spike timing in neocortical neurons. Science 268, 1503–1506. [PubMed: 7770778]

Major G, Polsky A, Denk W, Schiller J, and Tank DW (2008). Spatiotemporally graded NMDA spike/plateau potentials in basal dendrites of neocortical pyramidal neurons. J. Neurophysiol 99, 2584–2601. [PubMed: 18337370]

Major G, Larkum ME, and Schiller J (2013). Active properties of neocortical pyramidal neuron dendrites. Annu. Rev. Neurosci 36, 1–24. [PubMed: 23841837]

Makara JK, and Magee JC (2013). Variable dendritic integration in hippocampal CA3 pyramidal neurons. Neuron 80, 1438–1450. [PubMed: 24360546]

Mao T, Kusefoglu D, Hooks BM, Huber D, Petreanu L, and Svoboda K (2011). Long-range neuronal circuits underlying the interaction between sensory and motor cortex. Neuron 72, 111–123. [PubMed: 21982373]

Markram H, Lübke J, Frotscher M, Roth A, and Sakmann B (1997). Physiology and anatomy of synaptic connections between thick tufted pyramidal neurones in the developing rat neocortex. J. Physiol 500, 409–440. [PubMed: 9147328]

Markram H, Wang Y, and Tsodyks M (1998). Differential signaling via the same axon of neocortical pyramidal neurons. Proc. Natl. Acad. Sci. U S A 95, 5323–5328. [PubMed: 9560274]

Meyer HS, Wimmer VC, Hemberger M, Bruno RM, de Kock CPJ, Frick A, Sakmann B, and Helmstaedter M (2010). Cell type-specific thalamic innervation in a column of rat vibrissal cortex. Cereb. Cortex 20, 2287–2303. [PubMed: 20534783]

Meyer J, Maheshwari A, Noebels J, and Smirnakis S (2018). Asynchronous suppression of visual cortex during absence seizures in stargazer mice. Nat. Commun 9, 1938. [PubMed: 29769525]

Miyata M, and Imoto K (2006). Different composition of glutamate receptors in corticothalamic and lemniscal synaptic responses and their roles in the firing responses of ventrobasal thalamic neurons in juvenile mice: different composition of glutamate receptors in thalamic synapses. J. Physiol 575, 161–174. [PubMed: 16777934]

Neske GT (2016). The slow oscillation in cortical and thalamic networks: mechanisms and functions. Front. Neural Circuits 9, 88. [PubMed: 26834569]

Nevian T, Larkum ME, Polsky A, and Schiller J (2007). Properties of basal dendrites of layer 5 pyramidal neurons: a direct patch-clamp recording study. Nat. Neurosci 10, 206–214. [PubMed: 17206140]

Newkirk GS, Guan D, Dembrow N, Armstrong WE, Foehring RC, and Spain WJ (2021). Kv2.1 potassium channels regulate repetitive burst firing in extratelencephalic neocortical pyramidal neurons. Cereb. Cortex, bhab266. 10.1093/cercor/bhab266.

Oberlaender M, Boudewijns ZSRM, Kleele T, Mansvelder HD, Sakmann B, and de Kock CPJ (2011). Three-dimensional axon morphologies of individual layer 5 neurons indicate cell type-specific intracortical pathways for whisker motion and touch. Proc. Natl. Acad. Sci. U S A 108, 4188–4193. [PubMed: 21368112]

Oberlaender M, de Kock CPJ, Bruno RM, Ramirez A, Meyer HS, Dercksen VJ, Helmstaedter M, and Sakmann B (2012). Cell type-specific three-dimensional structure of thalamocortical circuits in a column of rat vibrissal cortex. Cereb. Cortex 22, 2375–2391. [PubMed: 22089425]

Omlor W, Wahl A-S, Sipilä P, Lütcke H, Laurenczy B, Chen I-W, Sumanovski LT, van't Hoff M, Bethge P, Voigt FF, et al. (2019). Context-dependent limb movement encoding in neuronal populations of motor cortex. Nat. Commun 10, 4812. [PubMed: 31645554]

Oviedo HV, and Reyes AD (2012). Integration of subthreshold and supra-threshold excitatory barrages along the somatodendritic axis of pyramidal neurons. PLoS One 7, e33831. [PubMed: 22457793]

Papoutsi A, Kastellakis G, Psarrou M, Anastasakis S, and Poirazi P (2014). Coding and decoding with dendrites. J. Physiol. Paris 108, 18–27. [PubMed: 23727338]

Petreanu L, Mao T, Sternson SM, and Svoboda K (2009). The subcellular organization of neocortical excitatory connections. Nature 457, 1142–1145. [PubMed: 19151697]

Ping X, and Jin X (2016). Transition from initial hypoactivity to hyperactivity in cortical layer V pyramidal neurons after traumatic brain injury *in vivo*. J. Neurotrauma 33, 354–361. [PubMed: 26095991]

Poleg-Polsky A (2015). Effects of neural morphology and input distribution on synaptic processing by global and focal NMDA-spikes. PLoS One 10, e0140254. [PubMed: 26460829]

Polsky A, Mel B, and Schiller J (2009). Encoding and decoding bursts by NMDA spikes in basal dendrites of layer 5 pyramidal neurons. J. Neurosci 29, 11891–11903. [PubMed: 19776275]

Poulet JFA, Fernandez LMJ, Crochet S, and Petersen CCH (2012). Thalamic control of cortical states. Nat. Neurosci 15, 370–372. [PubMed: 22267163]

Rah J-C, Bas E, Colonell J, Mishchenko Y, Karsh B, Fetter RD, Myers EW, Chklovskii DB, Svoboda K, Harris TD, et al. (2013). Thalamocortical input onto layer 5 pyramidal neurons measured using quantitative large-scale array tomography. Front. Neural Circuits 7, 177. [PubMed: 24273494]

Reike F, Bialek W, van Steveninck R, and Warland D (1999). Spikes: Exploring the Neural Code (MIT Press).

Richardson RJ, Blundon JA, Bayazitov IT, and Zakharenko SS (2009). Connectivity patterns revealed by mapping of active inputs on dendrites of thalamorecipient neurons in the auditory cortex. J. Neurosci 29, 6406–6417. [PubMed: 19458212]

Rothman JS, Cathala L, Steuber V, and Silver RA (2009). Synaptic depression enables neuronal gain control. Nature 457, 1015–1018. [PubMed: 19145233]

Sauerbrei BA, Guo J-Z, Cohen JD, Mischiati M, Guo W, Kabra M, Verma N, Mensh B, Branson K, and Hantman AW (2020). Cortical pattern generation during dexterous movement is input-driven. Nature 577, 386–391. [PubMed: 31875851]

Schiller Y (2002). Inter-Ictal- and Ictal-Like Epileptic Discharges in the Dendritic Tree of Neocortical Pyramidal Neurons. J. Neurophysiol 88, 2954–2962. [PubMed: 12466421]

Schiller J, Major G, Koester HJ, and Schiller Y (2000). NMDA spikes in basal dendrites of cortical pyramidal neurons. Nature 404, 285–289. [PubMed: 10749211]

Schindelin J, Arganda-Carreras I, Frise E, Kaynig V, Longair M, Pietzsch T, Preibisch S, Rueden C, Saalfeld S, Schmid B, et al. (2012). Fiji: an open-source platform for biological-image analysis. Nat. Methods 9, 676–682. [PubMed: 22743772]

Scholl B, Wilson DE, and Fitzpatrick D (2017). Local order within global disorder: synaptic architecture of visual space. Neuron 96, 1127–1138.e4. [PubMed: 29103806]

Scholl B, Thomas CI, Ryan MA, Kamasawa N, and Fitzpatrick D (2021). Cortical response selectivity derives from strength in numbers of synapses. Nature 590, 111–114. [PubMed: 33328635]

Seibt J, Richard CJ, Sigl-Glöckner J, Takahashi N, Kaplan DI, Doron G, de Limoges D, Bocklisch C, and Larkum ME (2017). Cortical dendritic activity correlates with spindle-rich oscillations during sleep in rodents. Nat. Commun 8, 684. [PubMed: 28947770]

Shadlen MN, and Newsome WT (1994). Noise, neural codes and cortical organization. Curr. Opin. Neurobiol 4, 569–579. [PubMed: 7812147]

Shigematsu N, Ueta Y, Mohamed AA, Hatada S, Fukuda T, Kubota Y, and Kawaguchi Y (2016). Selective thalamic innervation of rat frontal cortical neurons. Cereb. Cortex 26, 2689–2704. [PubMed: 26045568]

Sreenivasan V, Esmaeili V, Kiritani T, Galan K, Crochet S, and Petersen CCH (2016). Movement initiation signals in mouse whisker motor cortex. Neuron 92, 1368–1382. [PubMed: 28009277]

Stern EA, Kincaid AE, and Wilson CJ (1997). Spontaneous subthreshold membrane potential fluctuations and action potential variability of rat cortico-striatal and striatal neurons in vivo. J. Neurophysiol 77, 1697–1715. [PubMed: 9114230]

Takahashi N, Kitamura K, Matsuo N, Mayford M, Kano M, Matsuki N, and Ikegaya Y (2012). Locally synchronized synaptic inputs. Science 335, 353–356. [PubMed: 22267814]

Takahashi N, Ebner C, Sigl-Glöckner J, Moberg S, Nierwetberg S, and Larkum ME (2020). Active dendritic currents gate descending cortical out-puts in perception. Nat. Neurosci 23, 1277–1285. [PubMed: 32747790]

Takahashi N, Moberg S, Zolnik TA, Catanese J, Sachdev RNS, Larkum ME, and Jaeger D (2021). Thalamic input to motor cortex facilitates goal-directed action initiation. Curr. Biol 31, 4148–4155.e4. [PubMed: 34302741]

Taxidis J, Pnevmatikakis EA, Dorian CC, Mylavarapu AL, Arora JS, Samadian KD, Hoffberg EA, and Golshani P (2020). Differential emergence and stability of sensory and temporal representations in context-specific hippocampal sequences. Neuron 108, 984–998.e9. [PubMed: 32949502]

Ujfalussy BB, Makara JK, Branco T, and Lengyel M (2015). Dendritic nonlinearities are tuned for efficient spike-based computations in cortical circuits. eLife 4, e10056. [PubMed: 26705334]

Ujfalussy BB, Makara JK, Lengyel M, and Branco T (2018). Global and multiplexed dendritic computations under in vivo-like conditions. Neuron 100, 579–592.e5. [PubMed: 30408443]

Vesuna S, Kauvar IV, Richman E, Gore F, Oskotsky T, Sava-Segal C, Luo L, Malenka RC, Henderson JM, Nuyujukian P, et al. (2020). Deep posteromedial cortical rhythm in dissociation. Nature 586, 87–94. [PubMed: 32939091]

Wang Y, Markram H, Goodman PH, Berger TK, Ma J, and Goldman-Rakic PS (2006). Heterogeneity in the pyramidal network of the medial prefrontal cortex. Nat. Neurosci 9, 534–542. [PubMed: 16547512]

Highlights

- Testing how dendritic branches integrate natural patterns of spine stimulation

- It is the combined input rate to a proximal branch that drives supralinear boosting

- Neuron and branch types encode input based upon their distinct rate sensitivities

- Rate-based synaptic integration may preferentially amplify slow network oscillations
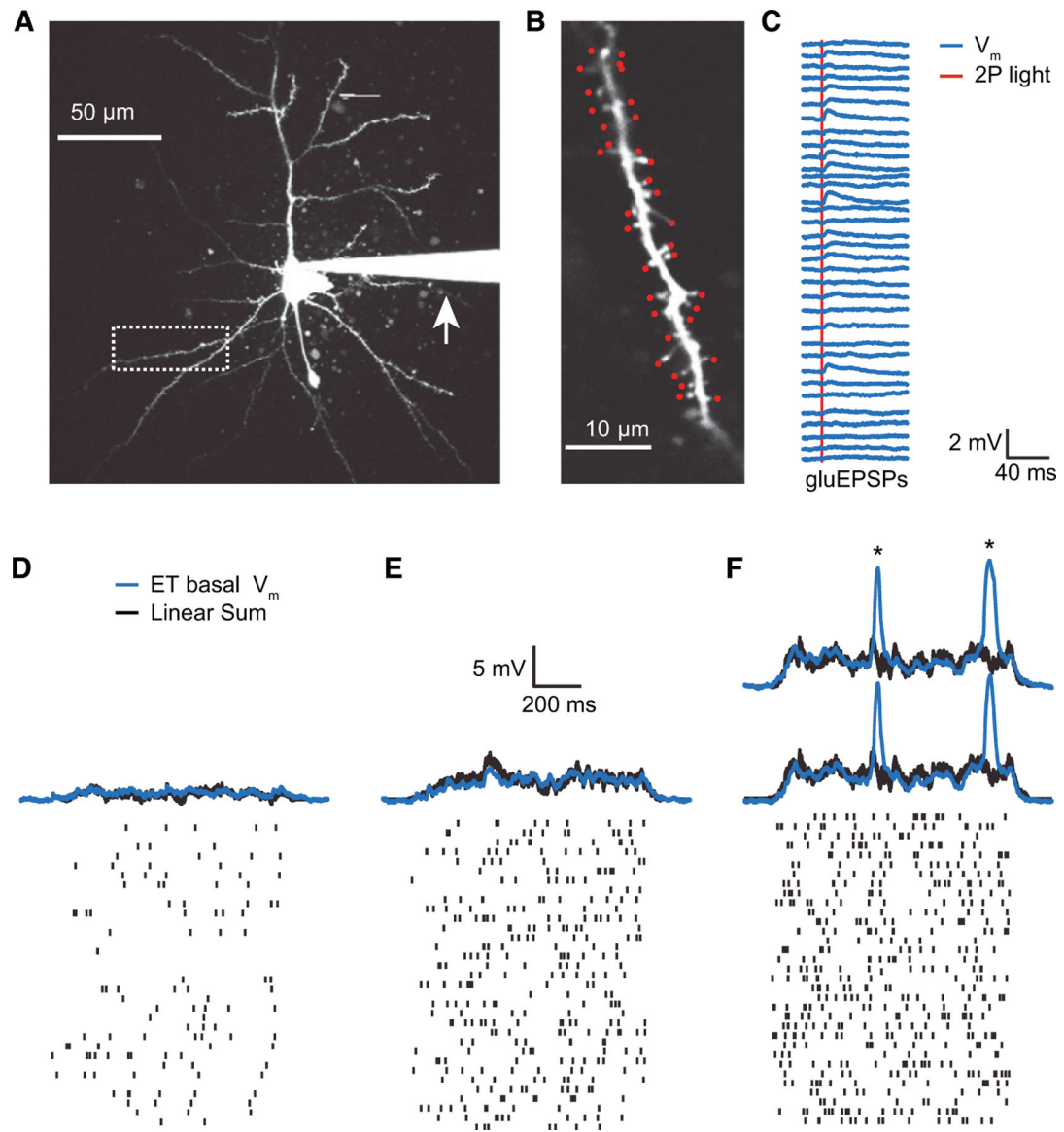
Figure 1. Branch integration in the proximal dendrites of L5 pyramidal neurons in the motor cortex

(A) Photomicrograph of an ET L5 pyramidal dendritic arbor with a somatic whole-cell recording electrode (arrow).

(B) Enlarged and rotated image of the basal dendrite marked with a dashed rectangle from (A) with glutamate photolysis sites near individual spines (red circles).

(C) Glutamate-evoked EPSPs (gluEPSPs) from two-photon photolysis of MNI-glutamate (2P-glu) using 0.2 ms light pulses (red line) from the 34 individual spines targeted in (B) (blue traces).

(D) Continuous spine stimulation of the ET basal dendrite shown in (A). Spines were repeatedly activated with 2P-glu (0.2 ms light pulses) with a Poisson distribution of stimulus times for each spine. The mean light pulse rate at each spine was 4.3 Hz. Bottom: raster plots of Poisson distributed light pulse times for each spine. Top: evoked voltage responses (blue traces) superimposed with calculated linear sum (black traces).
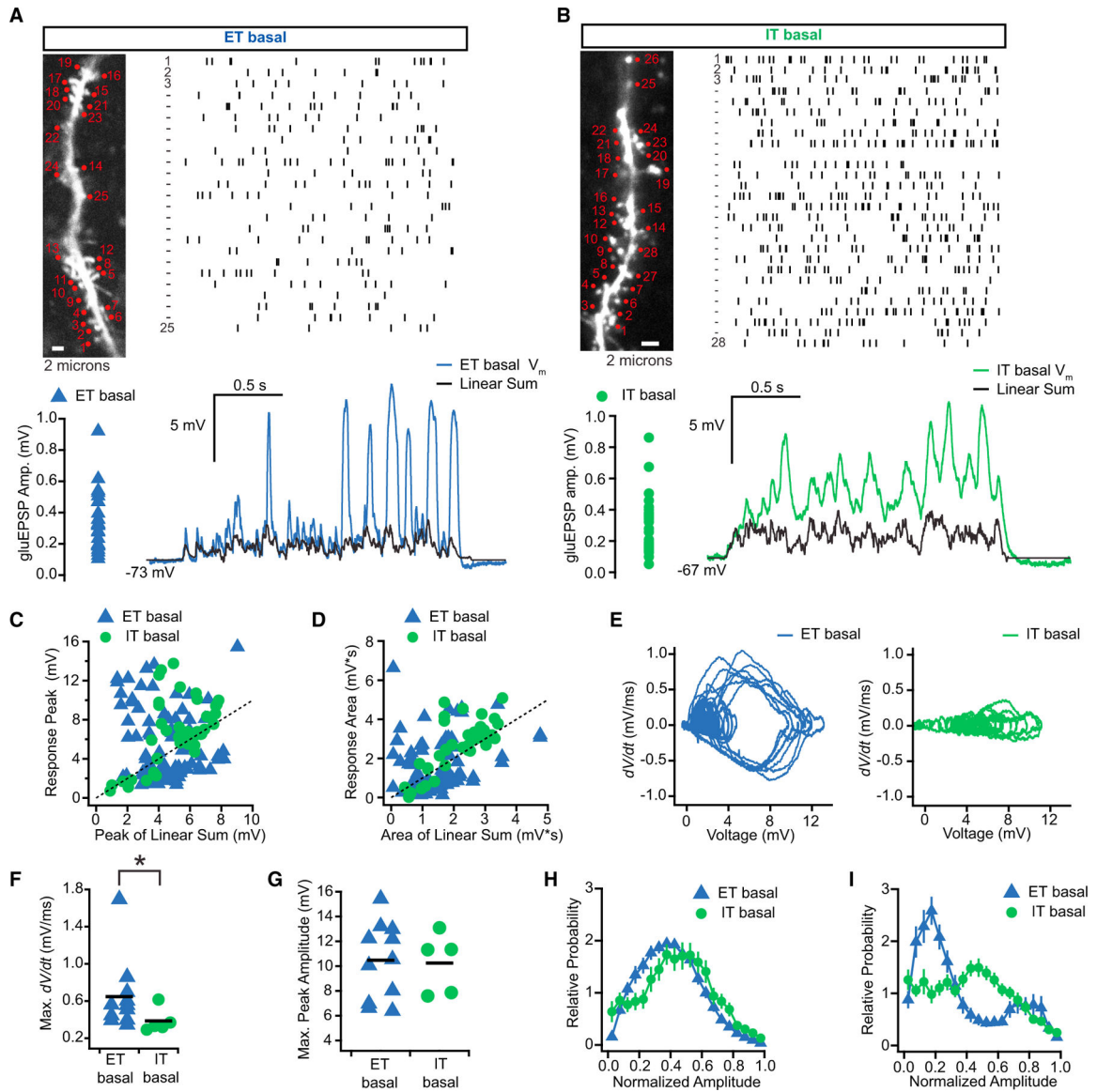
(E) Continuous spine stimulation of the same dendrite at a mean rate of 9.3 Hz per spine.

(F) Two repeated trials with a frozen sequence of continuous spine stimulation at 13.9 Hz per spine. Each trial evoked voltage responses with reproducibly timed supralinear events (marked by asterisks).

Figure 2. Comparing dendritic integration evoked by continuous spine stimulation in ET versus IT basal dendrites

(A) Representative response of an ET basal dendrite to continuous spine stimulation. Upper left, photomicrograph of the dendrite with 25 spines targeted (photolysis sites marked by red circles). Upper right, raster plot of the Poisson distributed stimulus times for each spine (mean rate of 4.5 Hz). Lower left, amplitudes of the individual gluEPSPs from each spine when stimulated in isolation. Lower right, voltage response of the ET basal dendrite (blue trace) superimposed with the calculated linear sum (black trace).

(B) Representative response from an IT basal dendrite (green trace) to 28 spines activated at a mean rate of 9.4 Hz per spine. Similar arrangement of panels as in (A), but voltage responses are shown in green.

(C) The peak amplitude of the voltage response plotted against the peak of the calculated linear sum for every continuous spine stimulation trial (mean total input rates of 70–451 Hz; 15–43 spines targeted for each dendrite) for ET basal dendrites (blue triangles, 90 trials

in 11 dendrites) and IT basal dendrites (green circles; 41 trials in 5 dendrites). The linear amplitudes are shown by the dashed black line. Trials were considered supralinear if the evoked response was >0.5 mV above the linear sum (denoted by the gray dashed bar).

(D) Measured area of the voltage response plotted against the area of the linear sum for the same trials in (C).

(E) Phase plots of change in voltage (*dV/dt*) versus voltage above rest from the ET (blue) and IT (green) trials shown in (A and B) (see STAR Methods for calculation of *dV/dt*).

(F) The maximum *dV/dt* elicited across all stimulus trials during continuous spine stimulation was significantly higher in ET (blue triangles) versus IT(green circles) basal dendrites (Wilcoxon rank test, $p < 0.05$).

(G) The maximum peak amplitude elicited for the same stimulus trials and dendrites in (F).

(H) Histograms of the distribution of voltages for ET and IT basal dendrites for the subset of stimulation trials with no supralinear response (at or below dashed line from (C): 43 trials from 9 ET basal dendrites and 14 trials from 4 IT basal dendrites). Voltages were normalized by subtracting the baseline and dividing by the maximal response.

(I) Histograms of the distribution of voltages of the supralinear trials (>0.5 mV above dashed line in (C) for ET basal dendrites (blue triangles, 47 trials from 11 dendrites) and IT basal dendrites (green circles, 27 trials from 5 dendrites).

Scale bars are standard errors of the mean.
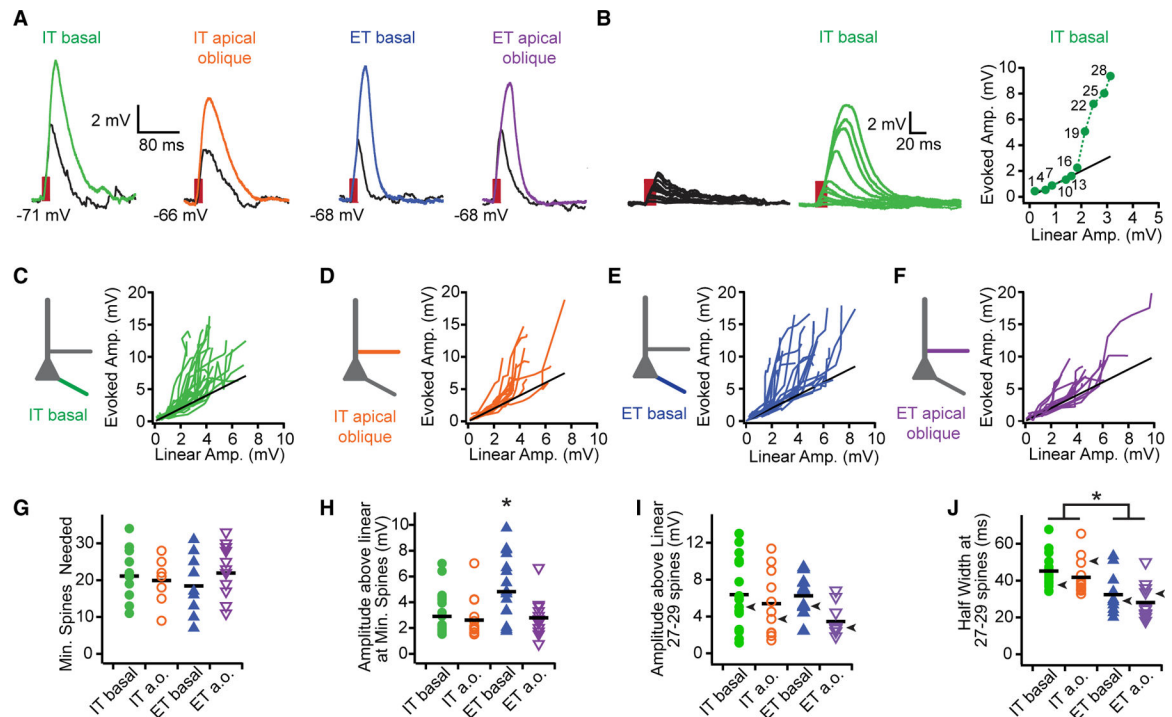
Figure 3. Near-simultaneous multi-spine activation in ET and IT neuron proximal dendrites

(A) Representative responses from near-simultaneous 2P-glu at multiple spines. The 0.2 ms light pulses were delivered once for each spine in random order at 2 kHz (red bar): IT basal dendrite (28 spines, green trace), IT apical oblique dendrite (29 spines, orange trace), ET basal dendrite (28 spines, blue trace), and ET apical oblique dendrite (28 spines, purple trace). Calculated linear sum for each dendrite is shown in black.

(B) Superimposed evoked responses to 2P-glu at 2 kHz for 1–28 spines (incremented by 3 spines) on an IT basal dendrite (green, middle). Left, the calculated linear sums (black traces) matching each stimulation. Right, plot of the peak amplitude of the evoked response (green circles with number of stimulated spines indicated) versus the peak amplitude of the linear sum (black line).

(C–F) Plots of evoked amplitude as in (B) versus linear amplitude for 21 IT basal dendrites (green) (C); 11 IT apical oblique dendrites (orange) (D); 19 ET basal dendrites (blue) (E); and 14 ET apical oblique dendrites (purple) (F). The maximum number of activated spines varied (from 16 to 46, see Figure S6) depending on the number of spines clearly visible in plane on each dendrite.

(G) The minimum number of spines necessary to elicit a supralinear evoked response at 2 kHz did not significantly depend upon neuron ($F_{(1,58)} = 0.402$, $p = 0.529$) or dendrite type ($F_{(1,58)} = 0.001$, $p = 0.974$).

(H) The amplitude of the supralinearity (evoked response minus the linear sum) at the minimum number of spines necessary to evoke a supralinear response (i.e., spine counts) in (G) for each dendrite type. ET basal dendrites had significantly greater amplitudes than the other dendritic compartments ($p < 0.05$; effect sizes, 0.85–0.92).

(I) Amplitudes of the supralinearity evoked by 2 kHz stimulation for 27–29 spines in different dendrite types. While the mean amplitude response of ET apical oblique dendrites

was smaller than the other compartments, this did not reach significance (post-hoc analyses, p > 0.06). Representative traces from (A) are marked with arrowheads.

(J) Half-width of the responses evoked by 2 kHz stimulation of 27–29 spines were significantly longer in IT neurons regardless of branch type (cell type: $F_{(1,49)} = 25.92$, p < 0.001; branch type: $F_{(1,49)} = 2.56$, p = 0.1161; interaction between cell and branch: $F_{(1,49)} = 0.13$, p = 0.7232). For all statistical tests shown, the F and p values are from two-factor ANOVA followed by Tukey's multiple comparisons. Representative traces from (A) are marked with arrowheads.
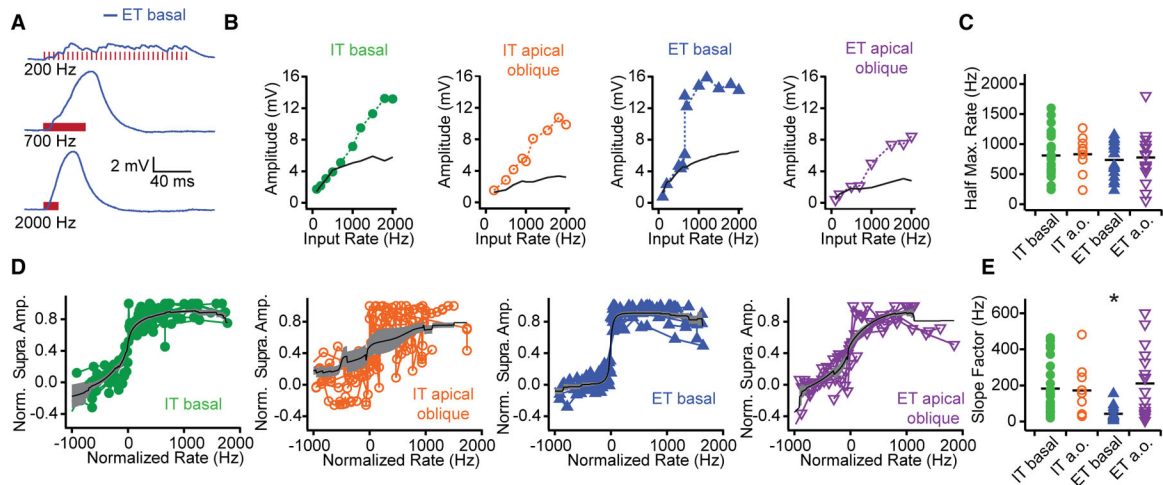
Figure 4. Input rate sensitivity of supralinear response in different proximal dendrite types

(A) Representative response of 31 spines in an ET basal dendrite (blue) stimulated at different interspine rates (top, 200 Hz; middle 700 Hz; bottom 2 kHz; timing of 0.2 ms light pulses shown in red).

(B) Representative plots of response amplitude as a function of interspine rate for a fixed number of spines. From left to right of an: IT basal dendrite (30 spines, green filled circles), IT apical oblique dendrite (34 spines, orange open circles), ET basal dendrite (27 spines, blue filled triangles), and ET apical oblique dendrite (34 spines, purple open triangles). The calculated linear sum for each dendrite is shown in black.

(C) The half-maximal rate of a sigmoid fit to the supralinear portion of the evoked responses versus the input rate does not significantly depend upon neuron type ($F_{(1,65)} = 0.4895$, $p = 0.487$) or dendritic compartment ($F_{(1,65)} = 0.115$, $p = 0.7354$), or interaction between cell type and branch type ($F_{(1,65)} = 0.01$, $p = 0.927$).

(D) Normalized amplitude versus normalized rate plots (see STAR Methods for calculation) from left to right for: IT basal (n = 25), IT apical oblique (n = 9), ET basal (n = 18), and ET apical oblique (n = 17) dendrites; same color and symbol scheme as in (B). Average of sigmoid fit curves (black) ± SE (gray) is shown for each plot.

(E) The slope factors of the sigmoid fits are significantly lower (steeper) in ET basal dendrites compared with the other three dendritic compartments ($F_{(1,65)} = 8.006$, $p < 0.01$; effect sizes = 1.25–1.46). The fixed number of spines used for calculating the rate sensitivity curves for each dendrite ranged from 19 to 37 (see STAR Methods for details). For all statistical tests shown, the F and p values are from two-factor ANOVA followed by Tukey's multiple comparisons.
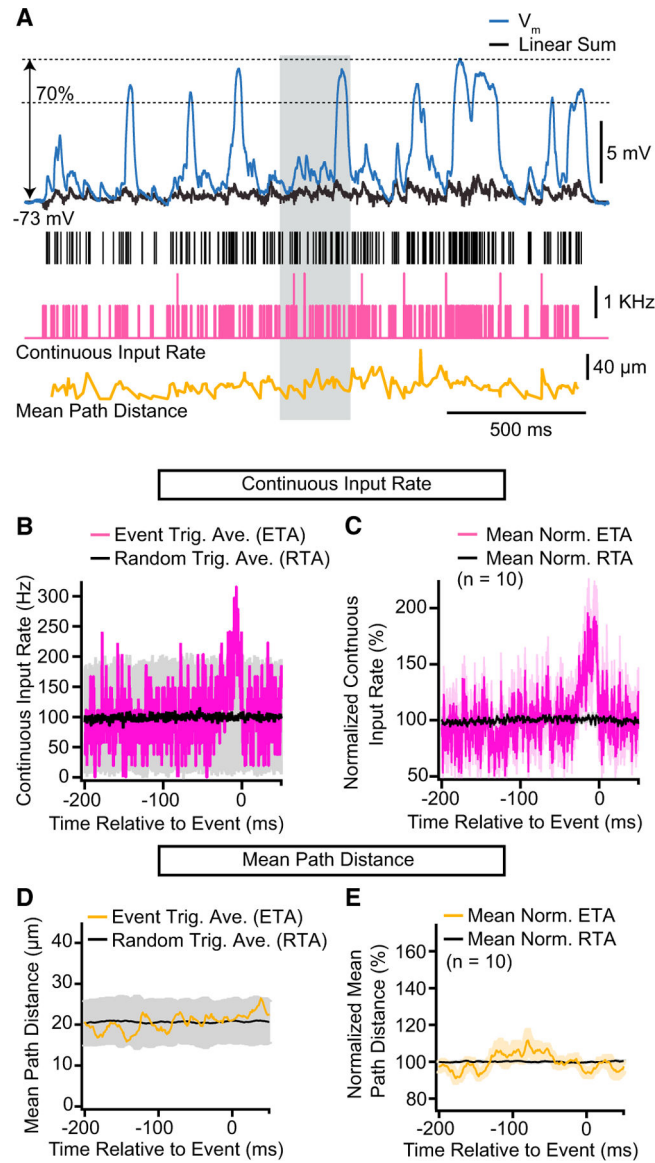
Figure 5. Event-triggered analysis of input parameters during continuous spine stimulation

(A) Top, a representative trace of the somatic voltage response (blue) and the calculated linear sum (black) of an ET neuron basal dendrite during continuous spine stimulation (4.3 Hz/spine 3 25 spines = mean total input rate of 107.5 Hz). Dashed line defines the voltage threshold (70% of the maximal voltage deflection above rest) for detecting supralinear event onset and shaded gray region showing width of representative window for calculating the event-triggered average (ETA). Collapsed raster plot of the stimulation times from all 25 spines shown below. Stimulation rate (estimated by a continuous input rate function, magenta) and the spatial clustering of the stimulated spines (estimated by the mean path distance, yellow) during continuous spine stimulation.

(B) The ETA (magenta) and the random-triggered average (RTA) (black with gray shading for standard deviation) of the rate for the dendrite shown in (A) (44 supralinear events across 6 trials, 2 s each trial).

(C) The average of the normalized rate ETAs (magenta) and RTAs (black) from 10 ET basal dendrites (7–56 events per dendrite, total of 267 supralinear events). Shaded lighter colors represent the standard error of the mean. A significant elevation in rate compared with the RTA prior to supralinear events was observed across a range of stimulus conditions (Student's t test, $p < 0.0001$, effect size = 1.12; mean rate per spine from 3 to 10 Hz/spine; 15–43 spines stimulated for each dendrite; mean total input rates from 110 to 364 Hz per dendrite).

(D) The ETA of the mean path distance (yellow) and corresponding RTA for the same dendrite from (A and B).

(E) The average of the normalized mean path distance ETA (yellow) and RTA path distances (black) from the same dendrites and events used in (C). Shaded lighter colors represent the standard error of the mean. See STAR Methods for details in calculating continuous input rate function, mean path distance, ETAs, RTAs, and their normalization.
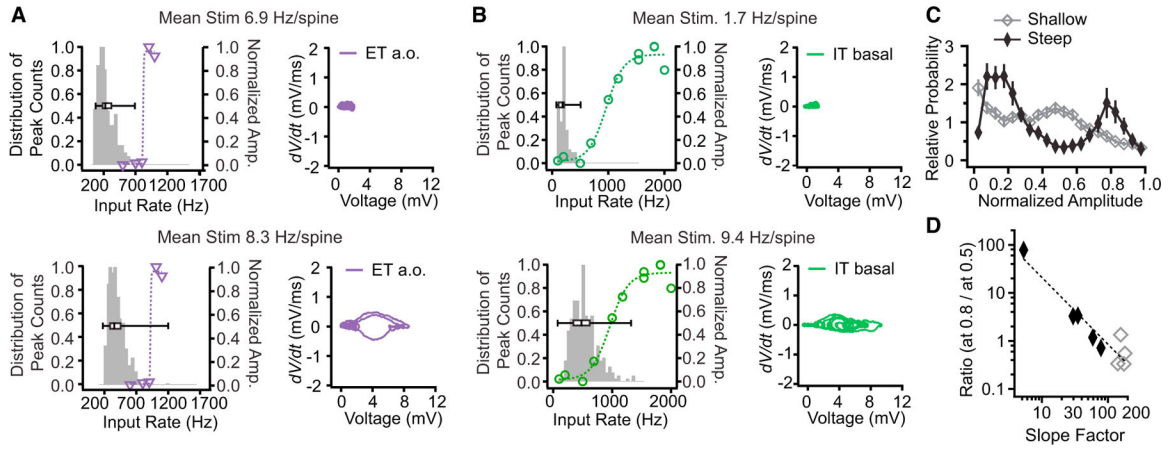
Figure 6. Rate sensitivity curves predict the voltage response during continuous spine stimulation

(A) The rate sensitivity curve informed how an ET apical oblique (purple, 30 spines) responded to different levels of continuous spine stimulation. Upper panels: continuous stimulation at a mean rate per spine of 6.9 Hz. Left, the steep rate sensitivity curve (30 spines, slope factor = 5.3 Hz, half-maximal rate = 821 Hz) overlaid on the distribution of the input rates during this trial (histogram of peaks in the continuous input rate function, gray bars; boxplot of distribution in black). Right, phase plots of the change in voltage in time (*dV/dt*) versus voltage of the response to this trial (see STAR Methods for calculation of *dV/dt*). Lower panels: the same complement of spines were stimulated at a higher mean rate per spine (8.3 Hz). The distribution of inputs rates (left) and the corresponding phase plot (right) during this trial.

(B) An IT basal dendrite (green, 42 spines) with a shallower rate sensitivity curve (slope factor = 156 Hz, half-maximal rate = 960 Hz) was tested for two different intensity levels of continuous spine stimulation. Upper panels: a weaker stimulation trial (1.6 Hz/spine). Lower panels: a higher stimulation trial (9.4 Hz/spine). Rate sensitivity curve overlaid with the distribution of inputs shown in left panels, phase plot of response to these inputs shown in the right.

(C) The distribution of normalized voltages during continuous spine stimulation trials with supralinear events (as done in Figure 2I) for dendrites with a steep rate sensitivity curve (steep, slope factor < 100 Hz, filled diamonds, n = 5 dendrites) versus a shallow rate sensitivity curve (shallow, slope factor > 100 Hz, open squares, n = 4 dendrites). Scale bars are standard errors of the mean.

(D) To compare the individual distributions that were averaged to make the ratio of the counts at 0.8 over the counts at 0.5 for each histogram were calculated and plotted against the slope factor for each dendrite's rate sensitivity curve. The linear fit (dotted line) of log-log values has $r^2 = 0.901$; same nine dendrites shown in (C).
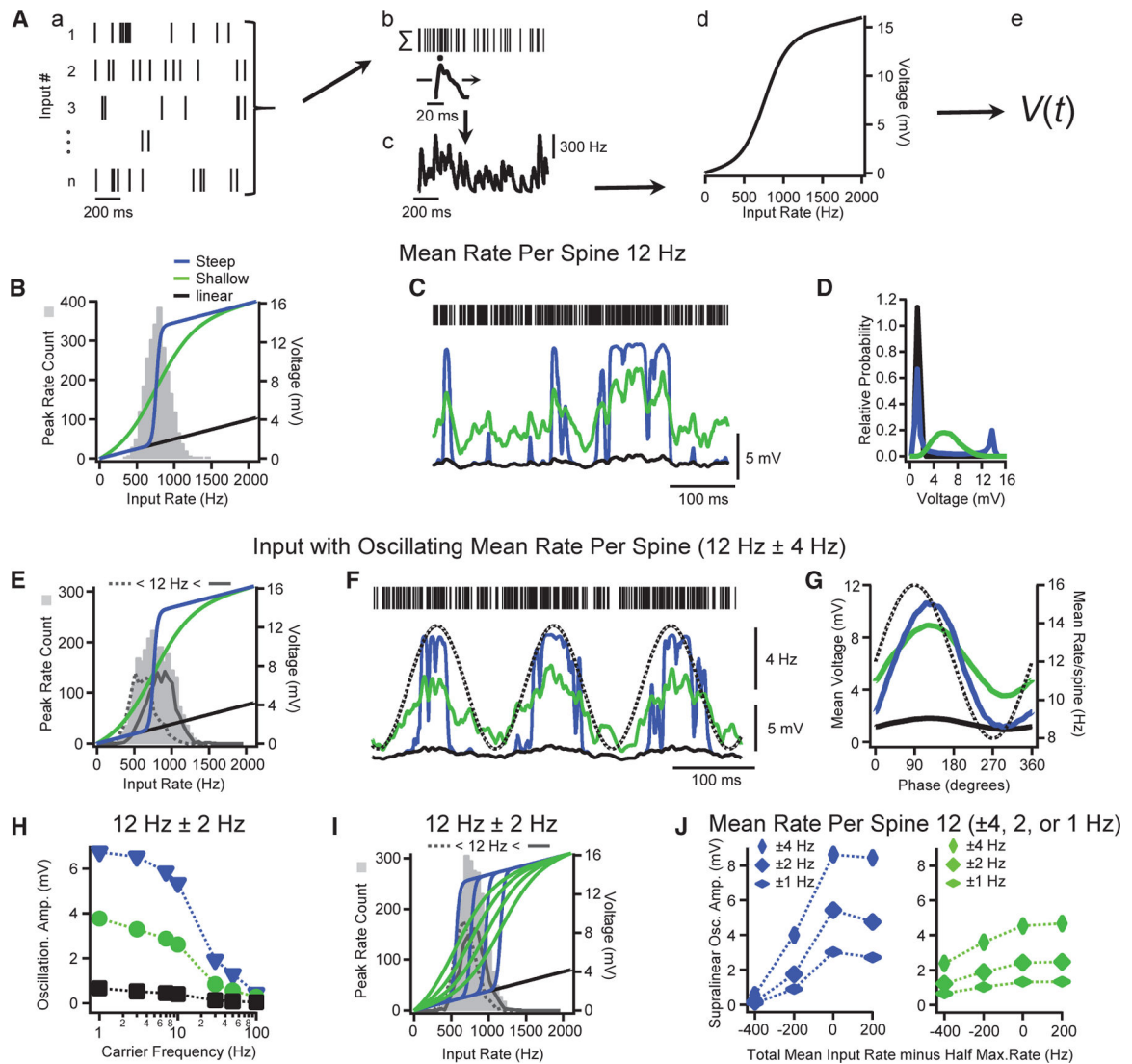
Figure 7. Amplification of low-frequency input oscillations in an input rate to voltage output model of branch integration

(A) The model, from left to right: (a) Poisson distributed stimulus events from n inputs were collapsed (b) into a single train, and convolved (d) with a smoothed and time-inverted waveform derived from the ETA calculated in Figure 5 to make (c) the continuous input rate function. (d) Rate sensitivity curves transformed the continuous input rate function into (e) membrane voltage as a function of time, $V(t)$; model details in STAR Methods.

(B) Rate sensitivity curves of three models (steep supralinear, blue; shallow supralinear, green; linear, black) are overlaid with the distribution of input rates (histogram of peaks in the continuous input rate function, gray bars) to all models during fixed mean rate stimulation (12 Hz/input, n = 60 inputs). Same color scheme is used throughout figure panels. Supralinear models had half-maximal rates (760 Hz) matching the midpoint of the distribution of input rates.

(C) $V(t)$ from the three models for a subportion of 50 s long simulations in response to 12 Hz/spine. Collapsed input train raster is shown above $V(t)$.

(D) Histograms of $V(t)$ from the three models to fixed mean input stimulation (from 50 s simulations).

(E) Sinusoidal oscillating inputs (mean rate/input of 12 ± 4 Hz on a carrier frequency of 7 Hz) overlaid with rate sensitivity curves of three models. Histograms of the subsets of input rate peaks above (solid gray line) and below (dashed line) 12 Hz also shown.

(F) $V(t)$ from the three models in response to oscillating inputs, superimposed with the change in the mean rate per input over time (dashed black line).

(G) Phase histograms showing the average $V(t)$ in phase with mean input rate (dashed black line) for each model (from 50 s simulations).

(H) Influence of carrier frequency upon the peak to trough amplitudes of the phase histograms for the linear (black boxes), shallow supralinear (green circles), and steep supralinear (blue triangles) models in response to 12 ± 2 Hz oscillating mean rate per input.

(I) Changing the half-maximal rate of the supralinear models. Steep and shallow rate sensitivity curves with half-maximal rates of 560, 960, and 1,160 Hz superimposed with a histogram of input rate peaks for an oscillating mean rate per input of 12 ± 2 Hz, same color scheme as (D).

(J) Peak to trough amplitude of the linear subtracted supralinear portion of the phase histograms for the steep (left, blue diamonds) and shallow (right, green diamonds) models across different strengths of input oscillation on a 7 Hz carrier frequency (see also Figure S8).

KEY RESOURCES TABLE

REAGENT or RESOURCE	SOURCE	IDENTIFIER
Experimental models: Organisms/strains		
Thy1h-eyfp (B6.Cg-Tg(*Thy1*-EYFP)-HJrs/J Mice	Jackson Laboratory	RRID: IMSR_JAX:003782
Etv1-egfp Tg(*Etv1*-EGFP)-BZ192Gsat/Mmucd Mice	Jackson Laboratory	RRID: MMRRC_011152-UCD
Charles River Swiss Webster Mice	Charles River	RRID: IMSR_CRL:024
Software and algorithms		
IgorPro 6.37	Wavemetrics	RRID: SCR_000325
Matlab R2012b (acquisition), R2019 (analysis)	Mathworks	RRID: SCR_001622
Prism	GraphPad	RRID: SCR_002798
Prairie View/Trigger Sync v. 2.0.5	Bruker	RRID: SCR_017142
ImageJ (FIJI)	Schindelin et al. https://doi.org/10.1038/nmeth.2019	RRID: SCR_002285; https://imagej.net/Downloads
Custom code for Simple Model	In Matlab and IgorPro environment	https://doi.org/10.5281/zenodo.5895134
Other		
Retrolabel Red Latex Microsphere Beads	Lumafluor	N/A